NEUROSCIENCE

Nicotinic regulation of local and long-range input balance drives top-down attentional circuit maturation

Elisa N. Falk[1,2,3,4,5], Kevin J. Norman[1,2,3,4,5]*, Yury Garkun[1,2,3,4,5]*, Michael P. Demars[1,2,3,4,5]*, Susanna Im[1,2,3,4,5], Giulia Taccheri[1,2,3,4,5], Jenna Short[1,2,3,4,5], Keaven Caro[1,2,3,4,5], Sarah E. McCraney[1,2,3,4,5], Christina Cho[1,2,3,4,5], Milo R. Smith[1,2,3,4,5], Hung-Mo Lin[6], Hiroyuki Koike[1,2,3,4,5], Julia Bateh[1,2,3,4,5], Priscilla Maccario[1,2,3,4,5], Leah Waltrip[1,2,3,4,5], Meaghan Janis[1,2,3,4,5], Hirofumi Morishita[1,2,3,4,5]†

Cognitive function depends on frontal cortex development; however, the mechanisms driving this process are poorly understood. Here, we identify that dynamic regulation of the nicotinic cholinergic system is a key driver of attentional circuit maturation associated with top-down frontal neurons projecting to visual cortex. The top-down neurons receive robust cholinergic inputs, but their nicotinic tone decreases following adolescence by increasing expression of a nicotinic brake, *Lynx1*. *Lynx1* shifts a balance between local and long-range inputs onto top-down frontal neurons following adolescence and promotes the establishment of attentional behavior in adulthood. This key maturational process is disrupted in a mouse model of fragile X syndrome but was rescued by a suppression of nicotinic tone through the introduction of *Lynx1* in top-down projections. Nicotinic signaling may serve as a target to rebalance local/long-range balance and treat cognitive deficits in neurodevelopmental disorders.

INTRODUCTION

The protracted nature of the frontal cortex maturation is important for establishing adult cognitive function, and this process is likely disrupted in neurodevelopmental and psychiatric disorders (*1*). Currently, little is known about the molecular mechanisms driving this developmental process because of the complexity of frontal cortex circuits and cognitive behavior. Identification of the drivers of circuit maturation in the context of cognitive behavior will likely point to therapeutic targets to reduce cognitive deficits shared across a range of disorders (*2*).

Of particular significance among frontal cortical circuits participating in cognition are top-down projections from frontal to sensory cortical areas. These neurons are recruited into brain-wide attentional networks conserved across species (*3*). In mice, frontal-sensory projection neurons from the anterior cingulate area (ACA) to the visual cortex (ACA_{VIS}) regulate the ability to detect visual features, a hallmark feature of visual attention (*4*). Attentional processing likely depends on developmental integration of local microcircuits and long-range inputs onto top-down frontal-sensory projection neurons up into adulthood. A recent study demonstrated that local excitatory drive onto ACA_{VIS} neurons decreases between adolescence (~p30 to p35) and adulthood (>p60) in mice (*5*). Attentional behavior in humans also continues to develop into adulthood (*6*–*8*). Moreover, deficits in frontal modulation of VIS activity are pervasively reported in neurodevelopmental disorders and often emerge between childhood and adulthood (*9*, *10*). However, the specific mechanisms driving the maturation of top-down circuit integration are poorly understood. As murine ACA_{VIS} neurons are known to causally regulate attention-related processing (*4*) and undergo a shift in local and long-range input balance following adolescence (*5*), mechanistic exploration of ACA_{VIS} top-down circuit maturation would facilitate an integrated understanding of molecular-, circuit-, and behavior-level mechanisms. Here, we aim to identify the molecular mechanism driving maturation of frontal circuitry associated with top-down ACA_{VIS} projection neurons in control of attentional behavior.

Neuromodulatory systems that are crucial for adult brain functions, however, are functionally in place early postnatally (*11*, *12*). Multiple neuromodulatory regions project directly to the ACA. Notably, a recent rabies virus–mediated tracing has revealed that basal forebrain (BF) region, where cholinergic neurons are located, is a major input source for adult ACA_{VIS} neurons (*13*). Here, we use circuit-selective methods in ACA_{VIS} neurons to examine the contribution of cholinergic system to top-down circuit maturation and attentional behavior. We also aim to assess whether these mechanisms are disrupted by a genetic risk of psychiatric disorders with neurodevelopmental origins and to determine whether targeting these mechanisms is sufficient to improve attentional function.

RESULTS

Postadolescent suppression of nicotinic tone in ACA_{VIS} neurons parallels with nicotinic brake *Lynx1* increase

ACA_{VIS} neurons undergo a shift in local and long-range input balance between adolescence and adulthood (*5*). To gain insight into a possible developmental contribution of the cholinergic neuromodulatory system on this late maturation period of ACA_{VIS} projection neurons, we first set out to assess in detail the direct inputs from BFs onto ACA_{VIS} neurons. Rabies virus–mediated input mapping demonstrated this neuromodulatory site as a monosynaptic input source for ACA_{VIS} neurons in the adult mice but did not characterize their

[1]Department of Psychiatry, Icahn School of Medicine at Mount Sinai, One Gustave L. Levy Place, New York, NY 10029, USA. [2]Nash Family Department of Neuroscience, Icahn School of Medicine at Mount Sinai, One Gustave L. Levy Place, New York, NY 10029, USA. [3]Department of Ophthalmology, Icahn School of Medicine at Mount Sinai, One Gustave L. Levy Place, New York, NY 10029, USA. [4]Mindich Child Health and Development Institute, Icahn School of Medicine at Mount Sinai, One Gustave L. Levy Place, New York, NY 10029, USA. [5]Friedman Brain Institute, Icahn School of Medicine at Mount Sinai, One Gustave L. Levy Place, New York, NY 10029, USA. [6]Department of Population Health Science and Policy, Icahn School of Medicine at Mount Sinai, One Gustave L. Levy Place, New York, NY 10029, USA.
*These authors contributed equally to this work.
†Corresponding author. Email: hirofumi.morishita@mssm.edu

cell type or identify their presence during adolescence (*13*). We thus performed detailed characterization of BF neurons projecting to ACA_{VIS} neurons through rabies virus–mediated input mapping in both adolescent and adult wild-type (WT) mice (Fig. 1A). We used a pseudotyped and genetically modified rabies virus [RbVd*G*(*EnvA*)-*eGfg*] to limit uptake to the ACA_{VIS} neurons expressing the cognate receptor, avian tumor virus receptor A (TVA), for cell entry, and rabies glycoprotein for cell exit (Fig. 1A). We found that both adolescent and adult mice show robust numbers of enhanced green fluorescent protein–positive ($eGFP^+$) input cells in the BF (Fig. 1B). We further demonstrated that most of the inputs from BF were choline acetyltransferase–positive cholinergic neurons (Fig. 1, C and D). These results suggest that BF cholinergic inputs are a major neuromodulatory source for ACA_{VIS} projection neurons present in adolescent development and persist into adulthood.

To further investigate the developmental contribution of cholinergic signaling to ACA_{VIS} projection neurons, we next examined whether cholinergic tone of ACA_{VIS} neurons changes between adolescence and adulthood. Given that cortical cholinergic tone is limited at nicotinic acetylcholine (ACh) receptors (nAChRs) in adulthood (*14*, *15*), we focused on developmental changes in nicotinic response. We measured ACh-evoked response in the presence of the muscarinic AChR blocker atropine in slice preparations (Fig. 2A). We found that nACh-evoked current detected in adolescent ACA_{VIS} projection neurons became significantly suppressed into adulthood (Fig. 2, B and C). Previous studies show that nACh tone of cortical neurons is suppressed after adolescence because of an increased expression of the glycosylphosphatidylinositol-anchored prototoxin, Lynx1, which brakes nicotinic signaling through nAChR interaction (Fig. 2D) (*14*, *16*). Thus, we examined the expression of *Lynx1* in ACA_{VIS} neurons following adolescence by in situ hybridization (Fig. 2E). In this experiment, ACA_{VIS} neurons were labeled by retro adeno-associated virus (AAV) encoding *Gfp* injected in VIS. We observed an increase in the percentage of *Lynx1*-expressing ACA_{VIS} neurons between adolescence and adulthood (Fig. 2F). Together, these data demonstrate a dynamic suppression of nicotinic tone in ACA_{VIS} neurons following adolescence, while a nicotinic brake, *Lynx1*, shows an increase in expression during this developmental period.

Lynx1 suppresses postadolescent nicotinic tone to shift local/long-range input balance onto ACA_{VIS} neurons

Having observed the increase in *Lynx1*-expressing ACA_{VIS} neurons and decrease in nACh tone following adolescence, we hypothesized that Lynx1 is a physiological brake of nicotinic tone in ACA_{VIS} neurons and contributes to the maturation of frontal cortex inputs to ACA_{VIS} projections. We performed whole-cell patch-clamp recordings from ACA_{VIS} neurons fluorescently labeled by retrobeads injected into VIS in adult *Lynx1* KO mice. Consistent with the known role of Lynx1 in suppressing nACh tone (*16*), ACA_{VIS} neurons in adult *Lynx1* KO mice exhibited an increased nicotinic tone compared to adult WT mice, which is comparable to the level of adolescent WT mice (Fig. 3, A to C). We next sought to determine whether ACA_{VIS} neurons also maintain adolescent-like input drive in the frontal cortex of adult *Lynx1* KO mice by measuring miniature excitatory postsynaptic current (mEPSC) and miniature inhibitory postsynaptic current (mIPSC) in ACA_{VIS} neurons. Compared to adult WT level, ACA_{VIS} neurons in adult *Lynx1* KO mice displayed significantly greater mEPSC frequency that resembled adolescent WT levels (*5*), while the mEPSC amplitude between the groups did not differ (Fig. 3, D to F). All groups display similar mIPSC frequency and amplitude of ACA_{VIS} neurons (Fig. 3, G to I). These data suggest that *Lynx1* deletion results in an adolescent-like hyperexcitatory input drive onto ACA_{VIS} neurons maintained even in adulthood.

Given that we observed developmental changes in presynaptic excitatory synaptic drive onto ACA_{VIS} neurons and that *Lynx1* has been previously reported to regulate dendritic spine dynamics (*17*, *18*), we next assessed the developmental contribution of *Lynx1* expression on dendritic spine maturation of ACA_{VIS} neurons in *Lynx1* KO and WT mice across development. Dendritic spines of ACA_{VIS} neurons at both adolescent and adult ages were visualized by an *eGfp*-encoding AAV with retrograde transduction capacity

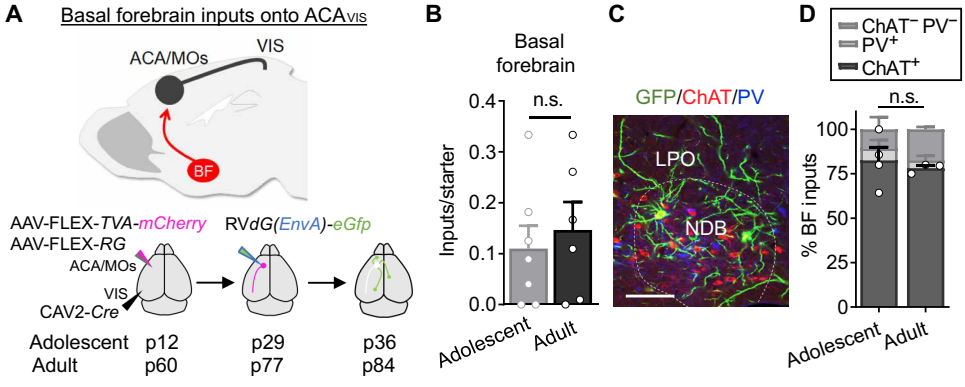

Fig. 1. BF cholinergic neurons provide robust inputs onto top-down ACA_{VIS} projection neurons. (**A**) Experimental overview of rabies virus–mediated input mapping of BF inputs onto ACA_{VIS} neurons in adolescent and adult mice. (**B**) Cre-dependent AAVs encoding *TVA-mCherry* and *Rb-G* were injected into ACA and retrograde CAV2-*Cre* into VIS. After 2.5 weeks, pseudotyped rabies virus was injected into ACA to allow for uptake of rabies virus in ACA_{VIS} neurons to express GFP in input cells over 1 week. AAV injections were initiated at p12 to capture inputs during adolescence (p36) and at p60 to capture inputs during adulthood (p84). (B) Number of BF inputs, when normalized to the number of mCherry + eGFP + starter cells in ACA (*t* test, $t_{11} = 0.5241$, $P = 0.611$; adolescent: seven mice; adult: six mice). n.s., not significant. (**C**) Representative image of immunohistochemical characterization of BF GFP + inputs by choline acetyltransferase (ChAT; red) and parvalbumin (PV; blue). Scale bar, 50 μm. LPO, lateral preoptic nucleus; NDB, nucleus of the diagonal band. (**D**) Inputs from BF are primarily $ChAT^+$ during adolescence (82.5%) and adulthood (78.17%), with a smaller PV^+ population (adolescent, 6.775%; adult, 4.467%), and ChAT-PV^- (adolescent, 10.73%; adult, 17.37%). The relative proportion of cell types does not differ between adolescent and adult groups (*t* test, $t_5 = 0.4904$, $P = 0.6446$; adolescent: four mice; adult: three mice).

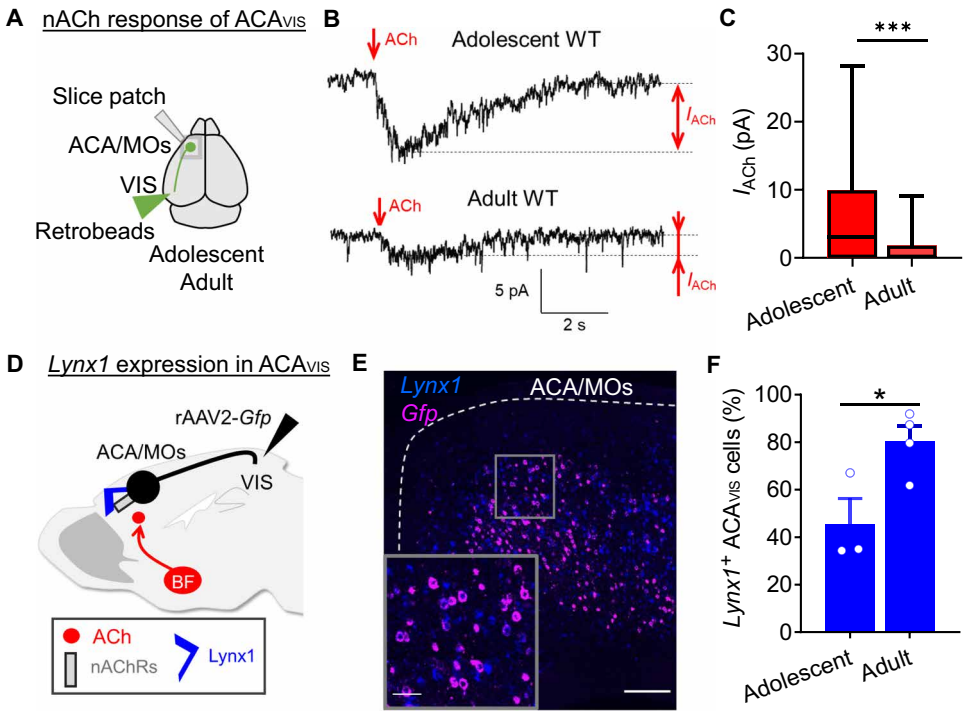

Fig. 2. Postadolescent decrease of nicotinic cholinergic tone in ACA_{VIS} neurons parallels with an increase in ACA_{VIS} neurons expressing *Lynx1*, a nicotinic brake. (**A** to **C**) nACh tone measurement by whole-cell patch-clamp recordings of ACA_{VIS} neurons. (A) ACA_{VIS} neurons are labeled with retrobeads for whole-cell patch-clamp slice recordings upon ACh puffing in the presence of atropine in adolescent (~p34: p32 to p36) and adult (~p77: p69 to p91) WT mice. (B) Representative recording traces of response to ACh puffing. (C) Adolescent ACA_{VIS} neurons show larger ACh-induced nicotinic currents compared to adult cells [linear mixed model (rank-based), $t_{59} = 4.05$, ***$P = 0.0002$; adolescent: 23 cells from 10 mice; adult: 28 cells from 10 mice). (**D** to **F**) *Lynx1* expression analysis. (D) ACA_{VIS} neurons were virally labeled with *Gfp* by retrograde rAAV2-*Gfp* injected in VIS to examine expression of a nicotinic brake, *Lynx1*, in adolescent (p31) and adult (p60) groups. (E) Representative image showing *Lynx1* mRNA (blue) in *Gfp* + ACA_{VIS} neurons (pink) (scale bar, 200 μm) by double in situ hybridization of *Gfp* and *Lynx1* in adult mouse. (F) The percentage of *Gfp* + ACA_{VIS} neurons expressing *Lynx1* increases between adolescence and adulthood (unpaired two-tailed *t* test, $t_5 = 2.896$, *$P = 0.0340$; adolescent: three mice; adult: four mice).

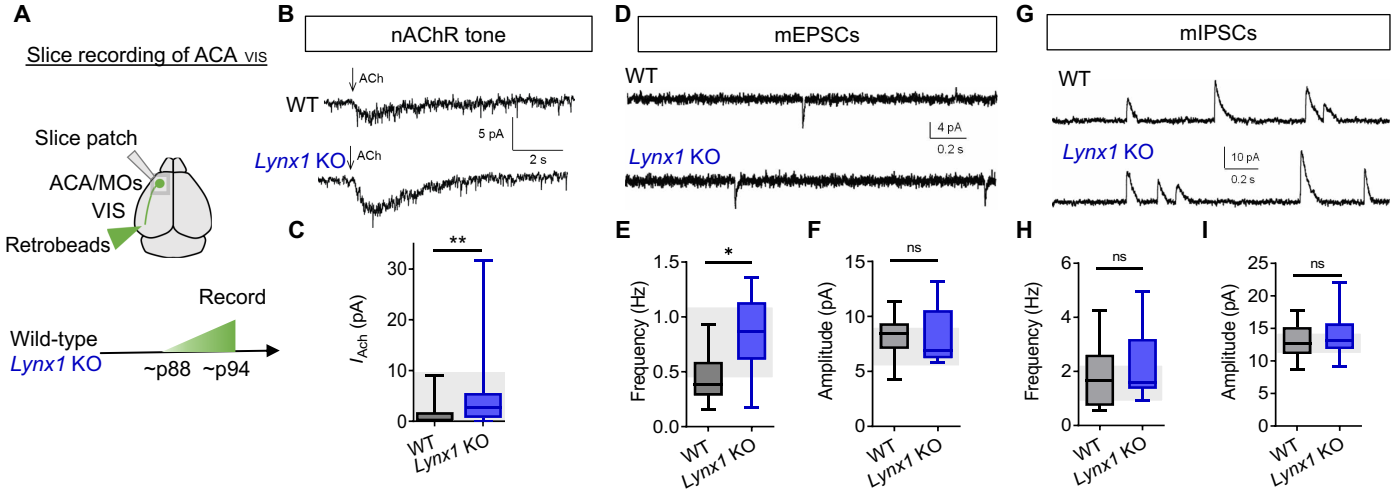

Fig. 3. *Lynx1* deletion leads to hypernicotinic tone and excess excitatory inputs onto ACA_{VIS} neurons in adulthood. (**A**) Experimental design: Whole-cell patch-clamp recordings from ACA_{VIS} neurons. (**B**) Representative traces of nACh response of ACA_{VIS} neurons in adult *Lynx1* KO and WT mice. (**C**) Adult *Lynx1* KO mice show increased nicotinic tone in ACA_{VIS} neurons compared to adult WT mice [linear mixed model (rank-based), $t_{28} = 3.33$, **$P = 0.0025$; adult WT: 28 cells per 10 mice; adult *Lynx1* KO: 36 cells per 12 mice]. Shaded region indicates the range of adolescent WT level [one to three quartiles from (*5*)]. (**D**) Representative traces of mEPSCs. (**E** and **F**) Adult *Lynx1* KO mice show increased mEPSC frequency compared to adult WT mice [(E) linear mixed model (rank-based), $t_{6.51} = 2.54$, *$P = 0.0410$] but no difference in mEPSC amplitude [(F) linear mixed model (rank-based), $t_{6.22} = -0.58$, $P = 0.5845$]. Adult WT: 15 cells per six mice; adult *Lynx1* KO: 10 cells per four mice. Shaded region, range of adolescent WT mice. (**G**) Representative traces of mIPSCs. (**H** and **I**) No changes in mIPSC frequency (H) or mIPSC amplitude (I) were observed between groups [linear mixed model (rank-based), $t_{11.6} = 1.14$, $P = 0.2789$ for frequency; $t_{8.37} = 0.61$, $P = 0.5551$ for amplitude; adult WT: 17 cells per eight mice; adult *Lynx1* KO: 16 cells per six mice]. Shaded region, range of adolescent WT mice.

introduced into VIS (Fig. 4A). We observed a significant age (adolescence and adult), genotype (*Lynx1* KO and WT), and spine-type (thin, stubby, and mushroom) interaction in dendritic spine density. In WT mice, between adolescence and adulthood, mushroom spine density increases, but thin spine density shows trending yet non-significant reduction, reflecting a late maturation of spines. However, in *Lynx1* KO mice, mushroom spine density does not increase, while thin and stubby spine density increases following adolescence. While a genotypic effect was not apparent at adolescent age, adult *Lynx1* KO mice displayed a higher density of thin and stubby spines compared to adult WT mice (Fig. 4, B and C), consistent with a higher excitatory input drive observed in adult *Lynx1* KO mice (Fig. 3E). The distinct developmental trajectory of spine maturation in *Lynx1* KO mice indicates a complex combination of late immaturity and deviation from normal developmental trajectory of spine maturations.

To next determine the circuit-level sources of increased inputs onto ACA_{VIS} projection neurons in adult *Lynx1* KO mice, we mapped brain-wide monosynaptic rabies inputs onto ACA_{VIS} neurons in adult WT and *Lynx1* KO mice (Fig. 5A). To allow for a direct quantitative comparison, we normalized the number of eGFP+ input cells by the number of double $eGFP^+$ $mCherry^+$ starter cells. ACA_{VIS} neurons in *Lynx1* KO adults displayed higher connectivity with local inputs from the ACA and adjacent secondary motor cortex (MOs) (Fig. 5, B and C) but no differences in distal long-range input connectivity (Fig. 5D) with similar distribution of input sources (fig. S1). When we calculated the relative percentage of total inputs coming from local areas compared to all other long-range distal brain regions for each animal, ACA_{VIS} neurons display a disrupted local/long-range input balance, with adolescent-like local hyperconnectivity in the adult *Lynx1* KO mice (Fig. 5E). These data reveal local hyperconnectivity consistent with an adolescent phenotype (*5*), suggesting a failure of ACA_{VIS} neurons to reduce local inputs in the absence of *Lynx1*. Together, these data suggest that post-adolescent increase of *Lynx1* expression is essential for shifting the balance of local and long-range input onto ACA_{VIS} projection neurons following adolescence by reducing excessive local excitatory inputs.

Lynx1 expression in ACA_{VIS} neurons from adolescence is essential for adult attentional behavior

Given that *Lynx1* deletion led to excessive local inputs onto ACA_{VIS} projection neurons, we then set out to determine whether this change in circuit connectivity is associated with behavioral consequences. Because ACA_{VIS} projection neurons can enhance the ability to detect visual features in VIS, a hallmark feature of visual attention (*4*), we hypothesized that *Lynx1* expression in ACA_{VIS} is necessary to establish adult top-down visual attentional behavior. We used a freely moving, visual detection task, the five-choice serial reaction time task (5CSRTT) (*19*) (fig. S2). 5CSRTT is known to require ACA activity (*20*) and demands more attention compared to a simpler CSRTT with less choice (*21*). Back-translated from the human continuous performance attention task in humans, the 5CSRTT has been extensively used to interrogate visual attention in rodents. This task assays sustained visual attention by requiring mice to maintain divided attention across five areas in anticipation of the presentation of a brief light stimulus that must be nose-poked to release a reward. Prior studies have shown that attention deficits can be measured quantitatively by decreases in accuracy (*19*).

We first examined whether germline deletion of *Lynx1* affects attentional behavior in adulthood (>p60). The adult *Lynx1* KO mice and control adult WT mice first underwent 5CSRTT training sessions to reach the criteria for testing (fig. S3A). During the testing sessions, we found that the genotype (*Lynx1* KO/WT) and stimulus duration (2, 1.5, 1, and 0.8 s) interaction for accuracy was suggestive (P = 0.08) but marginally not significant (fig. S3B). We therefore performed post hoc statistical tests as a secondary analysis for a hypothesis testing to further understand how genotype effects differed within subgroups. Post hoc analysis showed a significant reduction of accuracy in *Lynx1* KO mice only during 0.8-s stimulus duration trials, suggesting a preferential role of Lynx1 in the most attention-demanding condition. We did not observe any significant impact of *Lynx1* deletion in other behavioral readouts (fig. S3, C to H) including an independent assay to test for motivation, the progressive-ratio assay (fig. S3I), suggesting that reduced accuracy is not related to a loss of motivation. Performance deficits cannot also be attributed to vision deficits as adult *Lynx1* KO mice are reported to have normal

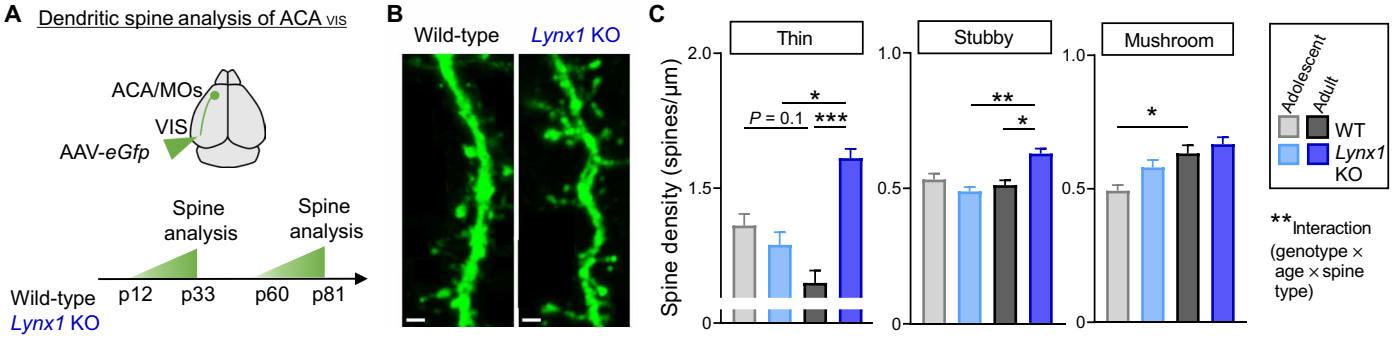

Fig. 4. *Lynx1* deletion alters developmental trajectory of dendritic spine maturation of ACA_{VIS} neurons. (**A**) Experimental approach to examine dendritic spines selectively in ACA_{VIS} projection neurons. A cross-sectional approach was applied to both *Lynx1* KO and WT mice for adolescent and adult time points. (**B**) Representative images of dendritic spines of ACA_{VIS} neurons. Scale bar, 1 μm. (**C**) Dendritic spine density of ACA_{VIS} neurons in WT mice and *Lynx1* KO mice during adolescence and adulthood. Doubly repeated measures linear mixed model: spine type × age × genotype interaction; $F_{2,20.6}$ = 6.42, $^{**}P$ = 0.0068. Thin: adult *Lynx1* KO versus adult WT; $F_{1,7.68}$ = 51.01, $^{***}P$ = 0.0001; adult *Lynx1* KO versus adolescent *Lynx1* KO mice; $F_{1,6.22}$ = 12.74, $^{*}P$ = 0.0111; adolescent WT versus adult WT; $F_{1,7.21}$ = 3.53, P = 0.1010. Stubby: adult *Lynx1* KO versus adult WT; $F_{1,9.85}$ = 7.45, $^{*}P$ = 0.0215; adult *Lynx1* KO versus adolescent *Lynx1* KO; $F_{1,9.12}$ = 14.02, $^{**}P$ = 0.0045. Mushroom: adolescent WT versus adult WT; $F_{1,7.38}$ = 9.90, $^{*}P$ = 0.0151. Adolescent WT: 68 dendrites per six cells per three mice; adult WT: 56 dendrites per six cells per three mice; adolescent *Lynx1* KO: 57 dendrites per six cells per three mice; adult *Lynx1* KO: 64 dendrites per six cells per three mice.

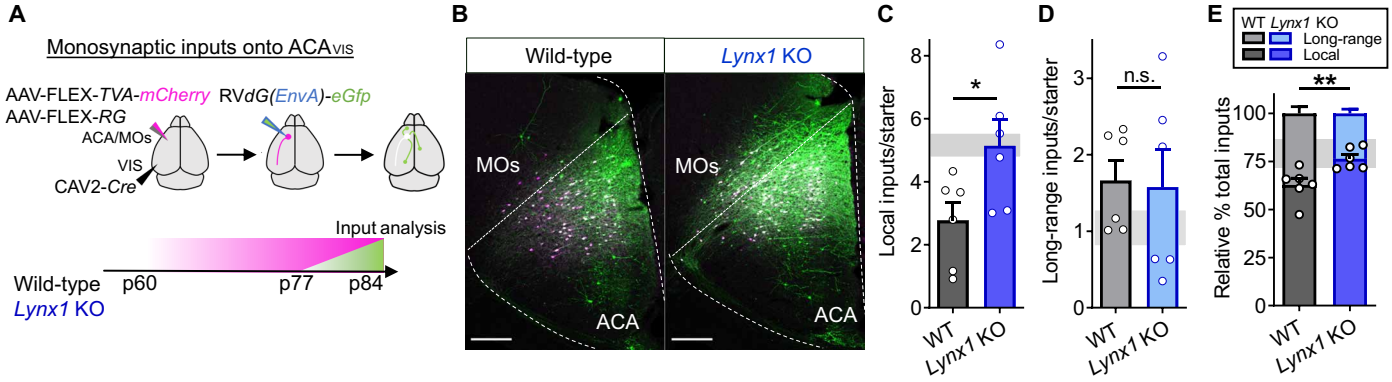

Fig. 5. *Lynx1* deletion leads to excess local inputs onto ACA_{VIS} neurons resulting in imbalanced local and long-range inputs in adulthood. (**A**) Experimental design to examine monosynaptic inputs onto ACA_{VIS} neurons in adult WT and *Lynx1* KO. (**B**) Representative images of local inputs (green) from ACA and secondary motor cortex (MOs) onto ACA_{VIS} projection neurons in white. Scale bars, 100 μm. (**C**) The number of inputs onto ACA_{VIS} is higher from local ACA and MOs brain regions in adult *Lynx1* KO mice compared to adult WT (*t* test, $t_{10} = 2.356$, $^*P = 0.0402$, six mice each) and comparable to adolescent WT level shown as a shaded region (*5*), (**D**) but not from long-range distal brain regions (*t* test, $t_{10} = 0.1515$, $P = 0.8826$, six mice each), leading to (**E**) disrupted local/long-range balance with excess local connectivity (*t* test, $t_{10} = 3.264$, $^{**}P = 0.0085$, six mice each) near an adolescent level shown as a shaded region.

visual acuity (*14*). Overall, these data support a hypothesis that *Lynx1* expression is necessary for proper visual attention behavior.

The mild phenotype in *Lynx1* KO mice on task performance may reflect compensational changes due to germline deletion of *Lynx1* throughout life. We thus next sought to determine whether attentional behavior deficits can be induced by a selective knockdown (KD) of *Lynx1* expression in ACA_{VIS} neurons from adolescence, when *Lynx1* expressing-ACA_{VIS} neurons normally increase. We used an intersectional viral approach to achieve *Lynx1* KD within ACA_{VIS} projection neurons by bilaterally introducing cre-dependent *Lynx1* KD vector (AAV-DIO-*Gfp-Lynx1* KD) into ACA and retrograde *Cre*-encoding virus in VIS (Fig. 6, A and B, and fig. S4A). Suppression of *Lynx1* expression was confirmed in $eGFP^+$ cells (Fig. 6, C and D). After going through the 5CSRTT training session (fig. S4B), the KD group showed disrupted visual attentional behavior in the 5CSRTT. This was marked by a decreased accuracy (Fig. 6E) without affecting other behavioral readouts (fig. S4, C to H) including an independent assay to test for motivation, the progressive-ratio assay (fig. S4I). These data reveal that expression of *Lynx1* from adolescence in ACA_{VIS} is necessary to establish adult visual attention abilities. The observed attention deficits can either be due to the effect of hypernicotinic tone during behavioral testing in adulthood and/or due to the late developmental role of Lynx1. To examine the former possibility, we acutely infused nAChR agonist (nicotine) through a bilateral cannula targeting ACA in adult WT mice during 5CSRTT. While we used the drug doses known to induce behavioral effect on other behaviors through ACA infusion (*22*), acute ACA nicotine infusion did not disrupt behavioral readouts of 5CSRTT (fig. S5). Collectively, these results suggest that the behavioral impact of *Lynx1* KD is less likely due to the ongoing nicotinic overstimulation during the task but may rather reflect the role of Lynx1 in regulating the maturation of ACA_{VIS} circuitry following adolescence.

A mouse model of fragile X syndrome shows local and long-range input imbalance and attentional deficits with hypernicotinic tone

Having established that Lynx1-dependent suppression of nACh neuromodulation is essential for top-down circuit maturation and establishing adult attentional behavior, we next sought to determine whether the disruption of this process might be implicated in neurodevelopmental diseases. Informatics-based molecular matching is an effective approach to generate mechanistic hypotheses (*23*). We thus mapped the adult *Lynx1* KO cortical transcriptome signature (*23*) to publicly available genome-wide association study (GWAS) gene sets curated for neuropsychiatric diseases (*24*–*32*). (Fig. 7A). We found greatest enrichment of *Lynx1*-related signature with the gene set implicated in the autism spectrum disorder (ASD) GWAS dataset (Fig. 7B and table S2). We next sought to determine whether a tighter overlap of the *Lynx1* transcriptome signature exists with five more specific publicly available gene sets associated with monogenetic risk of ASD. Notably, there was statistically significant overlap with fragile X mental retardation protein (FMRP)–associated gene sets ($P < 0.0001$) and gene sets associated with Phelan-McDermid syndrome (*Shank3* mutation) ($P = 0.0181$), with no statistical overlap with gene sets associated with *22q11* deletion, tuberous sclerosis, or Rett syndrome (Fig. 7C and table S2).

Given the strongest overlap between *Lynx1*- and FMRP-associated signatures, we sought to determine whether the loss of function of *Fmr1* leads to failed top-down circuit network maturation and attentional behavior deficits similar to the adult *Lynx1* KO mice. The *Fmr1* KO mouse is considered as a valid model to examine the pathophysiology of fragile X syndrome as mutations observed in humans result in FMRP loss of function. To this end, we examined local and long-range input balance through rabies input mapping and attentional behavior on the 5CSRTT in the adult *Fmr1* KO mice (Fig. 7D). After confirming that *Fmr1* KO mice displayed similar numbers of starter cells to WT mice ($P = 0.2674$, unpaired two-tailed *t* test), monosynaptic input mapping revealed local/long-range imbalance with excess local connectivity, consistent with that of adolescent WT or adult *Lynx1* KO connectivity states (Fig. 7E). This balance deficit was driven by combinatorial nonsignificant changes in an absolute level of local inputs and long-range inputs [unpaired two-tailed *t* test, $P = 0.2941$ (local), $P = 0.3425$ (long-range)]. At the behavior level, we found that the adult *Fmr1* KO mice display a decrease in accuracy on the attention-demanding 5CSRTT (Fig. 7F and fig. S6). While we also observed an increase in omission and latency to reward in *Fmr1* KO mice, the progressive

ratio task showed no difference in break point, suggesting that increase in omission likely reflects attention deficits with lesser contribution of motivation deficits (fig. S6). The observed attention deficit is consistent with previous studies that collectively support attention deficits particularly as task difficulty increases in rodent *Fmr1* mutant models (*33*–*36*) and patients with fragile X syndrome (*37*, *38*).

Given that the circuit and behavioral phenotypes in adult *Fmr1* KO mice are similar to those of adult *Lynx1* KO mice, we speculated that both mouse lines may show downstream molecular convergence leading to similar circuit and behavior deficits. As previous studies did not detect significant decreases in *Lynx1* mRNA and protein expression in *Fmr1* KO cortical samples (*39*, *40*), we hypothesized that the *Fmr1* KO mice may have an increased nicotinic tone independent of *Lynx1* expression change in ACA_{VIS} projection neurons. We therefore performed whole-cell patch-clamp recording in ACA_{VIS} neurons labeled by retrobeads following ACh puffing alongside muscarinic blockade in adult *Fmr1* KO mice (Fig. 7G) and found an increased ACh-evoked nicotinic response in adult *Fmr1* KO compared to adult WT mice (Fig. 7, H and I). To gain insight into the source of hypernicotinic tone, we additionally performed pharmacological experiments. We found that an increased nicotinic response was more effectively blocked by non-α7 nAChR antagonist dihydro-β-erythroidine (DHβE) over α7 antagonist methyllycaconitine (MLA) (fig. S7). This result suggests contribution of heteromeric nAChR signaling to the hypernicotinic tone in the ACA_{VIS} neurons of *Fmr1* KO mice. Together, these data suggest that *Fmr1* KO mice have an immature pattern of local/long-range imbalance with attentional behavior consequences by accompanying a juvenile-like excessive nicotinic tone even in adulthood.

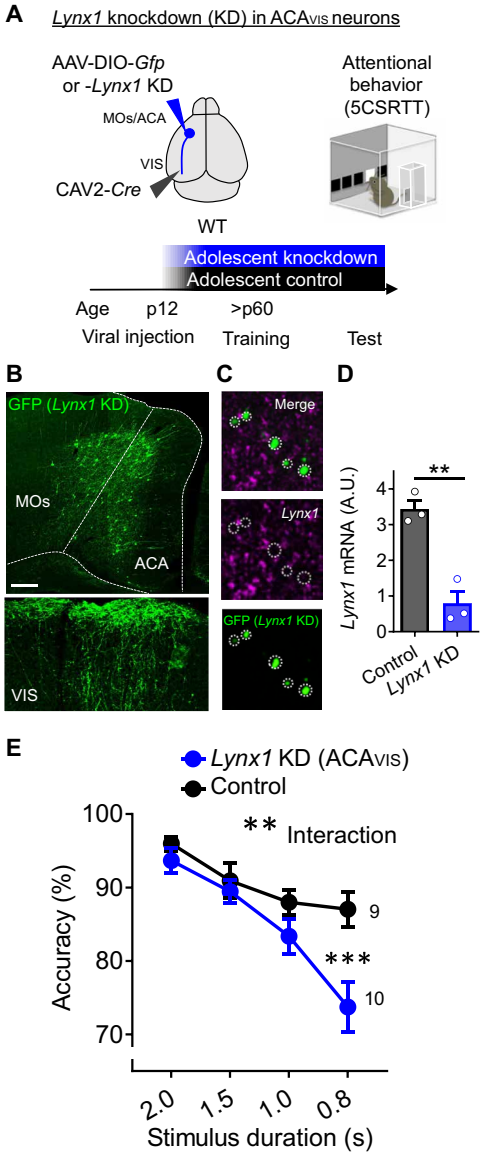

Fig. 6. *Lynx1* KD in ACA_{VIS} projection neurons from adolescence produces a visual attention deficit in adulthood. (**A**) Experimental design: To selectively knock down *Lynx1* expression in ACA_{VIS} projection neurons, WT mice were injected with a *Cre*-dependent AAV for *Lynx1* knockdown (KD) (or control cre-dependent *Gfp* AAV) into ACA and retrograde CAV2-*Cre* into VIS at p12, and attentional behavior training (5CSRTT) was initiated in adulthood. (**B**) Representative images of vector expression in ACA and VIS. Scale bar, 200 μm. (**C**) Validation of *Lynx1* KD by in situ hybridization. Representative images of GFP^+ virus expressing cells with no *Lynx1* mRNA. (**D**) Compared to control vector, expression of KD construct led to decreased *Lynx1* mRNA expression quantified by quantitative polymerase chain reaction (qPCR) (*t* test, $t_4 = 6.200$, $^{**}P = 0.0034$; control: three mice; *Lynx1* KD: three mice). A.U., arbitrary units. (**E**) *Lynx1* KD from adolescence decreased accuracy of 5CSRTT [two-way repeated measures analysis of variance (ANOVA), group × stimulus duration: $F_{3,51} = 5.723$, $^{**}P = 0.0019$; post hoc Šídák's multiple comparisons test (0.8 s): $^{***}P = 0.0002$; control: 9 mice; *Lynx1* KD: 10 mice].

Suppression of nicotinic tone in ACA_{VIS} neurons rescues local/long-range imbalance and attentional deficits in *Fmr1* KO mice

Having established that *Fmr1* KO mice have an increased nicotinic tone and display top-down circuit and behavior deficits similar to *Lynx1* KO mice, we hypothesized that Lynx1-mediated suppression of nicotinic tone in ACA_{VIS} projection neurons could ameliorate circuit and behavioral deficits in *Fmr1* KO mice. An intersectional viral approach was used to achieve *Lynx1* overexpression within ACA_{VIS} projection neurons by bilaterally introducing cre-dependent *Lynx1* overexpression vector into ACA and retrograde *Cre*-encoding virus in VIS (Fig. 8A). After validating viral overexpression of *Lynx1* in vivo (Fig. 8, B and C), whole-cell patch-clamp recording was performed from ACA_{VIS} projection neurons. We found that this vector expression in ACA_{VIS} neurons from adolescence resulted in a diminished nicotinic tone in *Fmr1* KO mice (Fig. 8D). Adult *Fmr1* KO mice were then assessed for local and long-range input balance by rabies virus–mediated monosynaptic labeling in adulthood following suppression of nicotinic tone in ACA_{VIS} neurons from adolescence (fig. S8A). We found that adult *Fmr1* KO mice selectively overexpressing *Lynx1* in ACA_{VIS} neurons from adolescence resulted in normalization of local and long-range input balance through the reduction of local inputs (Fig. 8E and fig. S8). Moreover, *Fmr1* KO mice with top-down *Lynx1* overexpression showed an increase of accuracy in 5CSRTT compared to *Fmr1* KO mice injected with a *Gfp* control vector (Fig. 8F and fig. S9) with no changes in other performance metrics (fig. S9). Collectively, these results demonstrated that suppression of nicotinic tone in ACA_{VIS} projection neurons by *Lynx1* overexpression from adolescence rescues local and long-range input imbalance and attentional deficits in *Fmr1* KO mice.

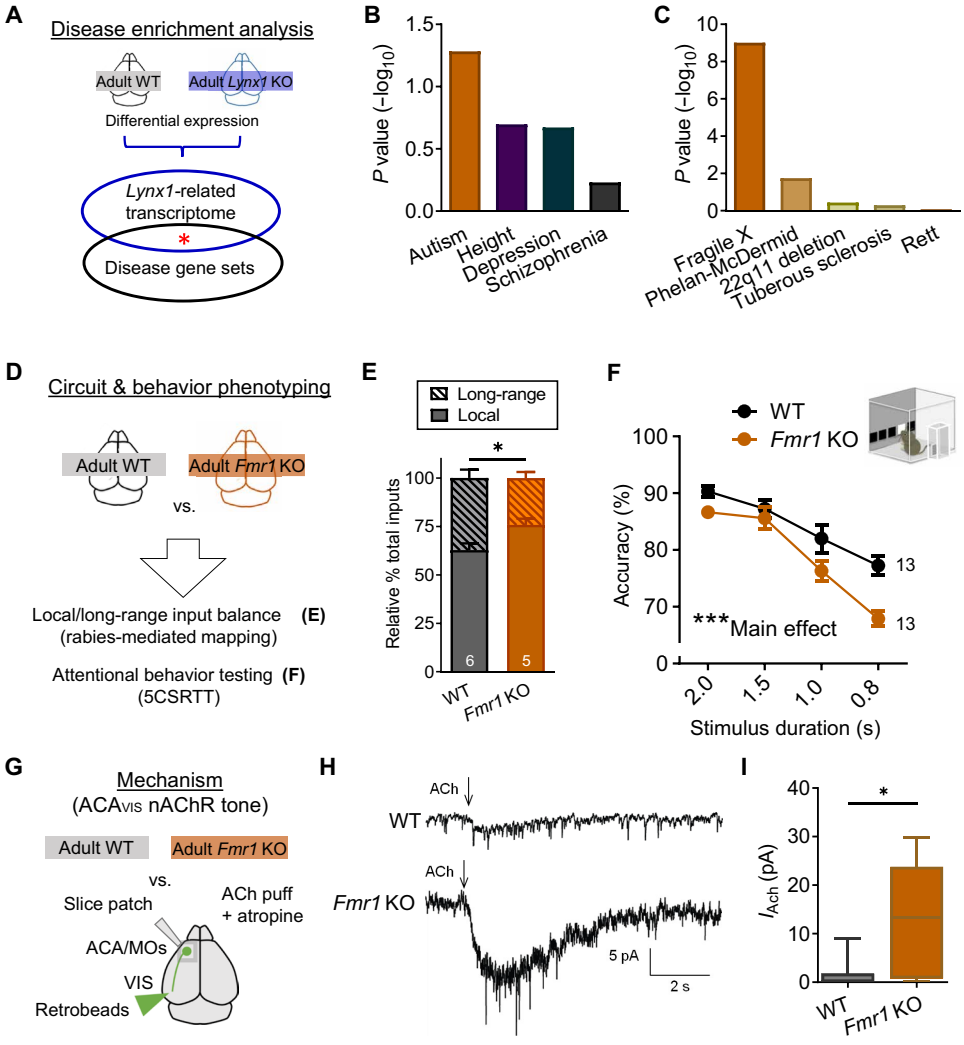

Fig. 7. Adult *Fmr1* KO mice displays attention deficits with disrupted local/long-range input balance and hypernicotinic tone of ACA_{VIS} neurons. (**A**) *Lynx1*-related transcriptional signature (differential expression of adult *Lynx1* KO and WT cortex) and GWAS gene sets were analyzed for enrichment. (**B**) *Lynx1* KO signature mapped to GWAS gene sets (ASD: $P = 0.0582$; height: $P = 0.2007$; depression: $P = 0.2127$; schizophrenia: $P = 1.0$). (**C**) *Lynx1* KO signature mapped to five autism-related gene sets [fragile X syndrome–related FMRP target genes: $P = 9.7 \times 10^{-10}$; Phelan-McDermid syndrome (*Shank3*KO): $P = 0.0181$; 22q11 deletion: $P = 0.3664$; tuberous sclerosis (*Tsc2*KO): $P = 0.5036$; Rett syndrome (*Mecp2* null mutation): $P = 0.8263$]. (**D**) Adult *Fmr1* KO mouse was screened for local/long-range input imbalance onto ACA_{VIS} neurons and attentional deficits. (**E**) Rabies virus–mediated input mapping showed increased local input connectivity ratio for ACA_{VIS} neurons in adult *Fmr1* KO mice (*t* test, $t_9 = 2.715$, $^*P = 0.0238$; WT: five mice; *Fmr1* KO: five mice). (**F**) Adult *Fmr1* KO mice showed reduced accuracy with the 5CSRTT [two-way repeated measures ANOVA, main effect (genotype): $F_{1,24} = 14.49$, $^{***}P = 0.0009$; WT: 13 mice; *Fmr1* KO: 13 mice]. (**G**) Adult *Fmr1* KO mice were evaluated for their nicotinic tone of retrobeads labeled ACA_{VIS} by whole-cell patch-clamp recordings. (**H**) Example trace recordings from ACA_{VIS} neurons upon ACh puffing in the presence of atropine. (**I**) Adult *Fmr1* KO mice show increased nicotinic responses in ACA_{VIS} neurons [linear mixed model (rank-based), $t_{6.94} = 3.40$, $^*P = 0.0116$; adult WT: 28 cells per 10 mice; *Fmr1* KO: 19 cells per 7 mice).

DISCUSSION

In this study, we set out to determine the mechanisms of frontal cognitive circuit maturation and found that dynamic regulation of nicotinic cholinergic tone is a major developmental driver of top-down attentional circuit and behavior. Further, we demonstrated that this process is disrupted in *Fmr1* KO mice but can be ameliorated by the top-down circuit-selective suppression of nACh tone (Fig. 9). Previous studies showed that nicotinic signaling is tightly balanced through a multilayered set of mechanisms across early development. nAChR signaling plays a trophic role in developing cortex through regulations of fetal choline level (*41*), cholinergic innervation from BF (*42*), and the expression level of nAChRs (*43*) toward the first three postnatal weeks in rodents (*44*, *45*). However, it was not clear to what extent the nACh system contributes to later stages of cortical maturation. An endogenous inhibitor of nAChRs, Lynx1, provides additional regulation of nicotinic signaling that is necessary to establish cognitive circuit. Our findings emphasize the key role of Lynx1 in late cortical maturation, extending the previously reported role of Lynx1 in limiting developmental cortical plasticity in sensory cortices (*14*, *17*, *18*, *46*) to establishing cognitive behavior in frontal association cortex.

At the circuit and behavior levels, our study suggests that Lynx1 acts as a key molecular mediator of late frontal circuit maturation and cognitive behavior. Specifically, we found that a number

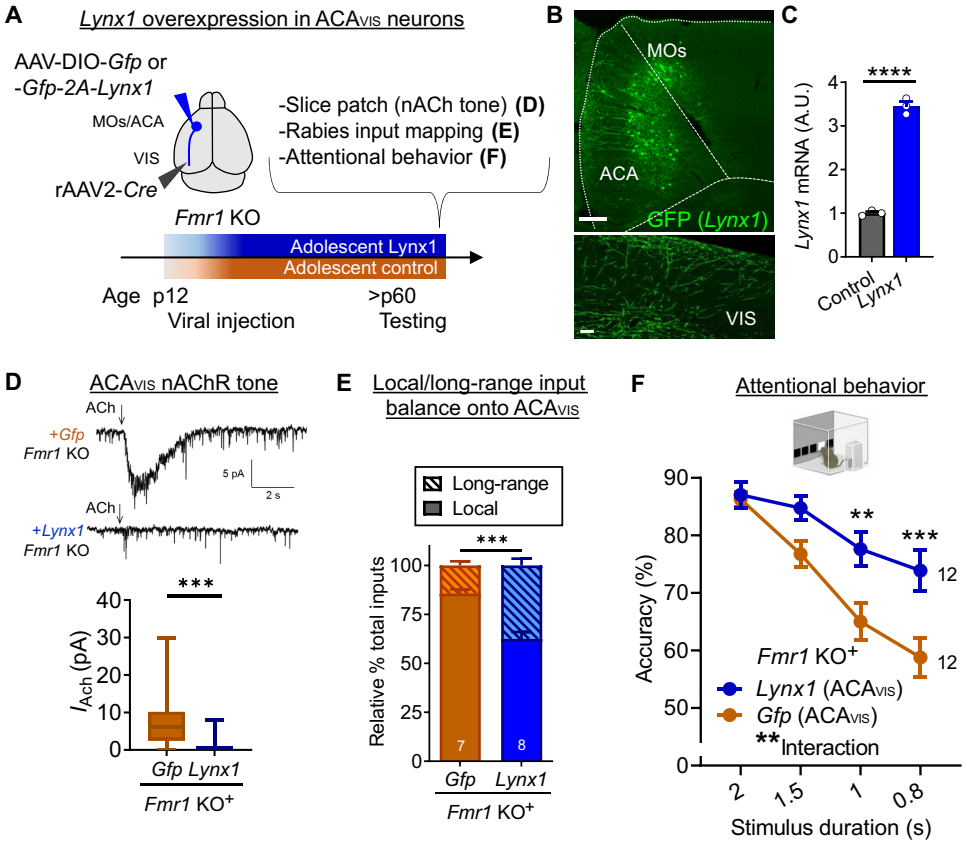

Fig. 8. Lynx1-mediated suppression of nicotinic tone from adolescence in *Fmr1* KO mice restores local/long-range input imbalance of ACA_{VIS} neurons and attentional behavior. (**A**) Experimental design: A *Cre*-dependent *Lynx1* overexpression or *Gfp* control AAV construct was injected in ACA, and retrograde rAAV2-*Cre* was injected in VIS at p12 in *Fmr1* KO mice. (**D**) nAChR tone, (**E**) local and long-range input balance, or (**F**) attentional behavior (5CSRTT) was assessed in adulthood. (**B**) Representative images showing GFP + ACA_{VIS} neurons in ACA (scale bar, 200 μm) and their terminals in VIS (scale bar, 5 μm). (**C**) Validation of AAV construct for cre-dependent *Lynx1* overexpression. qPCR shows cortical overexpression of *Lynx1* mRNA in vivo compared to noninjected native control (*t* test, $t_4 = 22.29$,****$P < 0.0001$, three mice each). (D) Top: Representative traces of whole-cell patch recording of ACA_{VIS} neurons overexpressing *Lynx1* or a control vector. Bottom: Nicotinic response in adult *Fmr1* KO mice [linear mixed model (rank-based), $t_{33} = 4.81$,***$P < 0.0001$; +*Gfp*: 23 cells per seven mice; +*Lynx1*: 20 cells per five mice]. (E) Rabies virus–mediated monosynaptic input mapping showed decreased percentage of local connectivity following *Lynx1* overexpression from adolescence in adult *Fmr1* KO mice (*t* test, $t_{13} = 5.453$,***$P = 0.0001$; +*Gfp*: seven mice; +*Lynx1*: eight mice). (F) Adult *Fmr1* KO mice with *Lynx1* overexpression in ACA_{VIS} neurons showed an increase in accuracy [two-way repeated measures ANOVA, group × stimulus duration: $F_{3,66} = 5.992$, **$P = 0.0011$; post hoc Šídák's multiple comparisons test (0.8 s): ***$P = 0.0006$; 1 s: **$P = 0.0055$; +*Lynx1*: 12 mice; +*Gfp*: 12 mice].

of ACA_{VIS} projection neurons expressing the nicotinic brake *Lynx1* increases following adolescence. This suppression of nicotinic tone is further associated with a late developmental shift in local/long-range input balance and establishment of adult attentional behavior. Previous studies demonstrated that mice lacking nAChRs show attention deficits (*47*). Thus, it was, at a glance, unexpected to observe attention deficits by Lynx1 KD as deletion of *Lynx1* is associated with elevated nAChR signaling (*16*) and arousal level (*48*). However, our series of experiments suggest that dampening of nACh tone by Lynx1 is necessary to limit local excitatory inputs following adolescence, which, in turn, may alter ACA_{VIS} neuron associated network dynamics. Imbalanced local/long-range circuitry in the absence of *Lynx1* may prevent finely tuned local computations in the frontal cortex necessary to effectively control distal sensory cortex during cognitive processing in a synchronized manner. As local inputs tend to preferentially target proximal dendrite (*49*), irrelevant local circuits may also interfere with a transmission from some of long-range inputs targeting distal dendrites to the soma. It should be also noted that attentional behavior deficits caused by *Lynx1* KD in ACA_{VIS} neurons can be due to resulting changes in visual input gain in the visual cortex in addition to input balance changes in ACA. One limitation of our study is that our experiments with *Lynx1* KD or overexpression from adolescence did not determine whether Lynx1 plays a role during adolescence or/and in adulthood. More temporally selective manipulations of *Lynx1* expression are necessary to answer these questions. Similarly, future studies are necessary to examine whether manipulations of *Lynx1* expression selectively in ACA_{VIS} projections modulate the local/long-range input balance onto ACA_{VIS} to establish a tighter link between local/long-range input balance and attentional behavior. Another limitation of this study is that we only assessed attentional behavior in adulthood due to the lengthy training and testing period (~2 months) required for touch screen–based 5CSRTT. Future studies should establish a short training protocol to permit assessment of attentional behavior during adolescence to examine to what extent the maturation of ACA_{VIS} circuitry is associated with attentional behavior changes.

Our study provides previously unrecognized insights into the pathophysiology of neurodevelopmental disorders by identifying that *Fmr1* KO mice display failed maturation of the ACA_{VIS} projection network

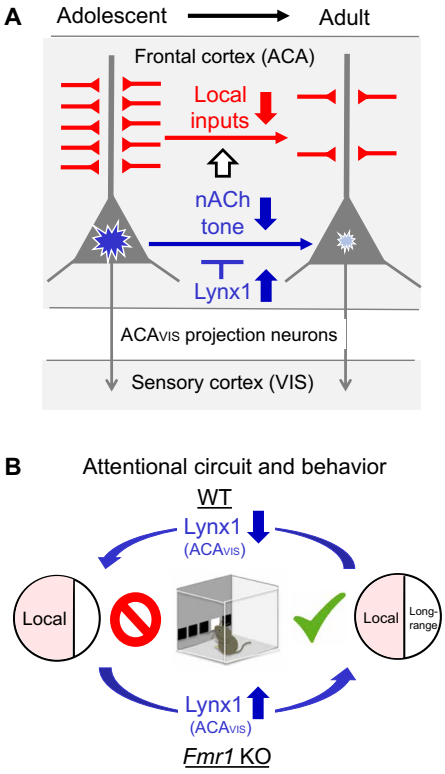

Fig. 9. Summary scheme. (**A**) Increased postadolescent *Lynx1* expression dampens nicotinic tone (blue blast mark), resulting in necessary reduction in excitatory local inputs (red) onto frontal ACA_{VIS} projection neurons. This process contributes to the shift of local and long-range input balance into adulthood. (**B**) Removal of *Lynx1* from ACA_{VIS} neurons disrupts the balance of local and long-range inputs onto ACA_{VIS} neurons with excessive local inputs and attention deficits. Conversely, hyperlocal inputs onto ACA_{VIS} and attention deficits in *Fmr1* KO mice can be prevented by overexpression of *Lynx1* in ACA_{VIS} projection neurons from adolescence.

leading to attention deficits due to hypernicotinic tone in ACA_{VIS} projection neurons. Our study pieces together the previous findings in rodent models of fragile X syndrome ranging from synaptic-level immaturity (*50*), connectopathy (*51*), to late emerging cognitive deficits (*33*–*36*, *52*) through shared functional deficits in nicotinic signaling. Given that *Fmr1* has various functions ranging from regulating the equilibrium between translation and transcription (*53*, *54*), trafficking mRNAs to dendrites without affecting the mRNA/protein level (*55*), to directing protein-protein interactions (*56*, *57*), future study is warranted to tease apart the cause of hypernicotinic tone in *Fmr1* KO mice. While cholinergic dysfunctions have been reported in *Fmr1* loss of function, it has been attributed to deficits in muscarinic AChR signaling (*58*–*60*). A previous pilot open-label trial for donepezil, an acetylcholinesterase inhibitor, reported that cognitive behavioral function of individuals with fragile X syndrome improved significantly (*61*), but more recent randomized placebo-controlled trials collectively support an insufficient effect of donepezil in improving cognitive behavior in these individuals (*62*, *63*). Our findings rather point to the dampening of nAChR signaling from adolescent period as an alternative target and time point for interventions. Long-range functional connectivity is commonly impaired in neurodevelopmental disorders and has been hypothesized to arise in the context of excessive short-range connections particularly in the context of ASD (*64*, *65*). Our study stresses a need for future studies to examine the balance between local and long-range connectivity across development in the context of neurodevelopmental disorders. Further, future studies are warranted to examine to what extent a regulation of nicotinic tone, perhaps through modulation of Lynx1-mediated actions, can serve as a possible therapeutic target for impairments of local and long-range input balance in general.

MATERIALS AND METHODS

Animals

Male C57BL/6 mice (Charles River Laboratories), *Lynx1* KO mice (gifted from N. Heintz at Rockefeller University) (*16*), and *Fmr1* KO mice (stock no. 003025, the Jackson Laboratory) were used. Mice were housed in a temperature and humidity-controlled vivarium under 12-hour light/dark cycle with ad libitum access to food and water. For behavior testing, mice were allowed access to water for 2 hours each day and maintained approximately 85 to 90% of respective baseline free-feeding weight (*5*). All animal protocols were approved by the Institutional Animal Care and Use Committee at Icahn School of Medicine at Mount Sinai.

Stereotactic surgery

Following procedures previously described in (*5*), mice were anesthetized with 2% isoflurane and head-fixed on a heating pad in a mouse stereotactic apparatus (Narishige International USA Inc.). Mice were isolated after surgery until fully awake and immediately returned to their home cage. VIS injection sites relative to lambda are the following: AP (+0.0 mm), ML (+3.0 mm), and DV (−0.4 mm); AP (+0.1 mm), ML (+2.85 mm), and DV (−0.4 mm); AP (+0.1 mm), ML (+3.15 mm), and DV (−0.4 mm). ACA injections sites relative to bregma are the following: AP (+0.7 mm), ML (+0.2 mm), and DV (−0.7 mm); AP (+0.2 mm), ML (+0.2 mm), and DV (−0.7 mm); AP (−0.3 mm), ML (+0.2 mm), and DV (−0.7 mm). For patch-clamp recordings, 500 nl of fluorescent retrobeads (Lumafluor Inc.) were injected into the VIS at least 24 hours before patch recordings to allow visualization of top-down projection neurons. A total of 350 nl of AAV5-hsyn-*eGfp*-WPRE (University of Pennsylvania Viral Core) was infused into VIS for dendritic spine labeling at p12 for the adolescent group and p60 to p75 for the adult group and allowed to express for 21 days. For rabies-mediated monosynaptic input mapping, 500 nl of a 1:1 volume mixture of AAV8-CA-FLEX-*RG* and AAV8-EF1a-FLEX-*TVAmCherry* (University of North Carolina Viral Core) was injected unilaterally in the ACA, and 500 nl of CAV2-*Cre* (Institut de Genetique Moleculaire de Montpellier) (for *Lynx1* KO/WT analysis) or rAAV2-*Cre* (Boston Children's Hospital Vector Core) (for *Fmr1* KO rescue analysis) was injected in VIS. For an introduction of rabies virus, 2.5 weeks later, 500 nl of pseudotyped *EnvA* RVdG-*Gfp* (for *Lynx1* KO and *Fmr1* KO study) or pseudotyped *EnvA* RVdG-*Bfp* (for *Fmr1* KO injected with AAV-*Gfp*/*Gfp*-*Lynx1* in ACA_{VIS}) (Salk Institute Viral Core) was injected into the ACA for local axonal uptake of rabies or VIS for distal axonal uptake of rabies. Mice were euthanized 7 days later. For behavioral studies, 500 nl of AAV8-DIO-*Lynx1* KD or AAV8-DIO-*Lynx1* (Custom Prep, Boston Children's Hospital) and 500 nl CAV2-*Cre* (for *Lynx1* KD) or rAAV2-*Cre* (Boston Children's Hospital Vector Core) (for *Lynx1* overexpression) were injected in the ACA and VIS, respectively, at p12 or p60.

Tissue preparation and histology

Following procedures previously described in (*5*), animals underwent transcardial perfusion with phosphate-buffered saline (PBS) followed by 4% paraformaldehyde (PFA) in PBS. For spine analysis, brains were postfixed in 4% PFA overnight and coronally sectioned at 35 μm for rabies input mapping and viral validation and 100 μm for dendritic spine analysis on a vibratome (Leica VT1000 S). For spine analysis, signal was enhanced by immunohistochemistry. Sections were placed into a blocking solution of 1% bovine serum albumin with 0.8% Triton X-100 in PBS on a rotating shaker for 1 hour at room temperature. The sections were then shaken for 48 hours at room temperature in primary antibody rabbit anti-eGFP (Invitrogen; 1:500), washed three times in blocking solution, and then shaken for 3 hours at room temperature in secondary antibody rabbit anti–Alexa Fluor 488 (Invitrogen; 1:400). The samples were then washed three additional times, twice in blocking solution and once in PBS with 0.01% sodium azide. All slices were then mounted on Superfrost Plus slides using Fluoromount-G mounting medium (SouthernBiotech) and coverslipped. Brains from rabies input mapping and AAV-injected brains for behavioral and other experiments were dissected, postfixed in 4% PFA for 3 hours, and cryoprotected in 30% sucrose in PBS for 24 to 48 hours before embedding in optimum cutting temperature (OCT; Tissue-Tek) and sectioning into 35-μm coronal slices using a cryostat (CM3050, Leica). For rabies input mapping, free-floating sections were washed in PBS before undergoing immunohistochemistry by 1-hour incubation in blocking solution (1% bovine serum albumin in 0.1% Triton X-100 in PBS) followed by overnight incubation with rabbit anti-eGFP antibody (1:1000 in blocking solution; Life Technologies) at room temperature. Sections were washed three times with blocking solution followed by incubation with Alexa Fluor 488–conjugated goat anti-rabbit antibody (Life Technologies) for 2.5 hours, washed three times in blocking solution, and mounted onto slides with 4′,6-diamidino-2-phenylindole (DAPI) Fluoromount-G (SouthernBiotech). Viral injections were validated using an LSM780 confocal microscope (Zeiss) in reference to the Paxinos and Franklin mouse atlas.

Monosynaptic input mapping

Following procedures previously described in (*5*), samples were imaged using an LSM780 confocal microscope (Zeiss). All slices around the ACA injection regions were stained for starter cell analysis. One of every eight serial sections was stained for input analysis. ImageJ [National Institutes of Health (NIH)] were used to process and analyze all images. Starter cells were defined as both $mCherry^+$ (>50% of soma pixels above 2 SD of the mean image mCherry fluorescence intensity) and $eGFP^+$ (>50% of soma pixels above 3 SD of the mean image GFP fluorescence intensity). Input cells were defined as $eGFP^+$ (>50% of soma pixels above 3 SD of the mean image eGFP fluorescence intensity). To determine the brain region location for all input and starter cells, all brain slices were registered to corresponding Allen Brain Institute coronal maps using anatomical landmarks visualized by DAPI counterstaining and tissue autofluorescence. First, we identified a coronal reference from the Allen Brain Atlas, which is a closest representation of each image. By visually comparing each image with a corresponding atlas, we then manually registered each brain region to each image by drawing boarders to each image using ImageJ. In a small minority of cases, assignment of input neurons to specific brain nuclei may be approximate if $eGFP^+$ cell bodies were located on borders between regions or when anatomical markers were lacking between directly adjacent regions. However, quantitative analyses of input tracing results were performed on anatomical classifications that were at least one hierarchical level broader (as specified by the Allen Brain Atlas) than the discrete brain regions to which input cells were assigned. Notably in many of these cases, directly adjacent nuclei fall together into the same hierarchical group. Both $eGFP^+$ input neurons and $eGFP^+$ $mCherry^+$ starter cells were manually counted using the "Cell Counter" plug-in in ImageJ. For the input analysis, we normalized the total number of input neurons in each brain to the total number of starter cells because the efficiency of rabies uptake by helper cells differed slightly across animals. The investigator performing these analyses remained agnostic of the group identities of animals during image analysis. For input mapping of *Fmr1* KO mice injected with AAV-*Gfp-Lynx1* or AAV-*Gfp*, quantification of input neurons was done with blue fluorescent $protein^+$ cells.

Slice electrophysiology

Following procedures previously described in (*66*), animals were decapitated under isofluorane anesthesia. Brains were quickly removed and transferred into ice-cold artificial cerebrospinal fluid (ACSF) of the following composition: 210.3 mM sucrose, 11 mM glucose, 2.5 mM KCl, 1 mM NaH_2PO_4, 26.2 mM $NaHCO_3$, 0.5 mM $CaCl_2$, and 4 mM $MgCl_2$. Acute coronal slices of ACA (300 μm) contained both hemispheres. Slices were allowed to recover for 40 min at room temperature in the same solution but with reduced sucrose (105.2 mM) and addition of NaCl (109.5 mM). Following recovery, slices were maintained at room temperature in standard ACSF composed of the following: 119 mM NaCl, 2.5 mM KCl, 1 mM NaH_2PO_4, 26.2 mM $NaHCO_3$, 11 mM glucose, 2 mM $CaCl_2$, and 2 mM $MgCl_2$. Patch-clamp recordings were performed from fluorescently labeled ACA neurons using borosilicate glass electrodes (3 to 5 megohms). Whole-cell voltage-clamp recordings were obtained with the internal solution containing 120 mM Cs-methanesulfonate, 10 mM Hepes, 0.5 mM EGTA, 8 mM NaCl, 4 mM Mg–adenosine triphosphate (ATP), 1 mM QX-314, 10 mM Na-phosphocreatine, and 0.4 mM Na–guanosine triphosphate (GTP). Current clamp recordings and ACh-evoked currents were obtained with the internal solution containing 127.5 mM *K*-methanesulfonate, 10 mM Hepes, 5 mM KCl, 5 mM Na-phosphocreatine, 2 mM $MgCl_2$, 2 mM Mg-ATP, 0.6 mM EGTA, and 0.3 mM Na-GTP. Neurons were included in the analysis if input resistance, series resistance, and membrane potential did not change more than 15% during the course of recordings. mIPSC and mEPSC were recorded in the presence of tetrodotoxin (TTX; 1 μM; Abcam). Miniature IPSC and EPSC were separated by holding the neuron at the reversal potential for EPSC or IPSC. To activate nicotinic receptors, ACh (1 mM) was dissolved in ACSF and loaded into a glass pipette connected to a Picospritzer II (Parker Instrumentation, Chicago, IL). Brief localized pulses of ACh (30 ms) were applied with a 60-s interpulse interval close to the soma of recorded neurons (within 50 to 60 μm) using a pressure of 10 psi. To block muscarinic ACh receptors, 1 μM atropine was bath-applied during the entire time of recordings. ACh-evoked currents were averaged across three applications and quantified as the distance between the local peak current and the baseline; the net ACh-evoked charge flow through the membrane was calculated by integrating the area above the baseline-subtracted postsynaptic current after ACh application. For pharmacological experiments, TTX,

MLA, and DHβE were diluted in ACSF to 1, 0.1, and 100 μM, respectively, and bath-applied.

Double fluorescence in situ hybridization

Following procedures previously described in (*67*), cloning for developing RNA probes for in situ hybridization was performed in a pBluescript II SK(−) vector using a polymerase chain reaction (PCR)–based isothermal DNA assembly method. Briefly, primers were designed to linearize the vector and create nonoverlapping overhang sequences. A second set of primers was used to amplify the gene of interest from complementary DNA (cDNA) derived from mouse cortex and create overhangs that were antisense to the vector overhang sequences. Assembly was achieved using Gibson Assembly master mix (New England Biolabs), and the resulting vector was used to transform NEB 5-alpha (New England Biolabs) competent cells. Positive (white) colonies were picked and cultured for miniprep. All miniprep DNA was subjected to restriction digest using Xho I enzyme (New England Biolabs) and examined for insert by gel electrophoresis. Properly inserted colonies were then amplified by 50-ml culture and subsequent midiprep using the HiSpeed Plasmid Midi Kit (QIAGEN). Plasmid DNA was then linearized using Xho I restriction digest and purified via phenol-chloroform and ethanol precipitation. Probes were synthesized using T3 RNA polymerase (Roche), the probe for *Lynx1* was labeled with fluorescein (fluorescein isothiocyanate; Roche), and the probe for *Gfp* was labeled with digoxigenin (DIG; Roche) for double in situ hybridization. Primers used for cloning include the following: Lynx1 (forward), CCGCTCGAGATCCTGTTACCCTGCGTGTG; *Lynx1* (reverse), CGGGATCCGCTTCCTCACATC CCACAG; *Gfp* (forward), GGTATCGATAAGCTTGATATCGTGAGCAAGGGCGAGGA; *Gfp* (reverse), CCCCGGGCTGCAGGAATCAGCTCGTCCATGCCGA. In situ hybridization of *Lynx1* and *Gfp* was performed as described previously (*67*). Briefly, mice were anesthetized with isofluorane and cervically dislocated. The brain was removed under ribonuclease-free conditions and quickly frozen in a standard mold with OCT in a chamber of 2-methylbutane on dry ice. After freezing, brains were transferred to −80°C until sectioning. Sectioning was performed on a cryostat at a thickness of 7 μm, and sections were immediately placed onto Tissue Path Superfrost Gold Plus slides (Thermo Fisher Scientific). Sections were allowed to dry and then stored in slide boxes at −80°C. For immunohistochemistry, anesthetized mice were transcardially perfused with cold 4% PFA dissolved in 0.1 M phosphate buffer. The brains were postfixed in 4% PFA at 4°C and cryoprotected in 30% sucrose solution. The frozen brains were sectioned into 40-μm coronal sections using a cryostat. Frozen sections on slides were thawed and fixed in 4% PFA. Following fixation, slides were washed in PBS and incubated for 10 min in acetylation buffer (0.2% HCl, 1.5% triethanolamine, and 0.28% acetic anhydride). Slides were again washed in PBS and then acclimated to hybridization buffer (50% formamide, 5× SSC, 2.5% yeast transfer RNA, 5% salmon sperm DNA, and 10% Denhardt's solution) in a humidity chamber. Following acclimation, the buffer was replaced with new hybridization buffer containing RNA probes and incubated overnight at 72°C in the humidity chamber. The next day, slides were washed 3 × 30 min in 0.2× SSC at 72°C and blocked in milk solution [tris-buffered saline (TBS) with 0.05% Tween 20 and 1% milk]. Slides were then incubated with milk containing anti-fluorescein-horseradishperoxidase antibodies (1:2000) for 2 hours at room temperature. Following incubation, slides were washed, subjected to TSA Plus dinitrophenyl (DNP) signal amplification (PerkinElmer), and again washed. Next, slides were again blocked with milk solution and incubated in milk solution containing anti–DIG-alkaline phosphatase and anti–DNP–keyhole limpet hemocyanin–488 (both 1:1000; Roche) for 2 hours at room temperature. Following incubation, slides were washed and acclimated to TBS (pH 8.0) and then incubated in fast red solution (Roche) for 1 hour at room temperature. Last, slides were washed in water and coverslipped using CC/Mount solution (Sigma-Aldrich).

Imaging and quantification

For in situ hybridization colocalization analysis of *Lynx1* and *Gfp*, imaging was performed using LSM780 confocal microscopes (Zeiss) and was processed and analyzed using ImageJ software (NIH). A threshold of light intensity value 9509 was set to define *Lynx1* signal and 710 to define *Gfp* signal. Gfp^+ cells were counted as $Lynx1^+$ if they contained one or more puncta of *Lynx1* signal. Percentage of colocalization of *Lynx1* and *Gfp* was calculated by $Lynx1^+$ Gfp^+ cells/total number of Gfp^+ cells. This analysis was done for eight images per animal, from three to four individual mice in each group. For the viral spread validation of mice, mice that had completed behavior testing underwent transcardial perfusion, and slices were collected at specific bregma areas (from 2.06 to −1.78) using the Allen Brain Atlas to analyze the anterior-posterior spread of virally infected cells. Images were acquired using the EVOS FL Imaging System (Thermo Fisher Scientific). Slices were imaged using a 4× lens, and, to ensure consistency across imaging sessions, power was set at 100%. To generate viral spread diagrams, all groups were assigned two levels representing increasing levels of signal intensity. The first level represented the minimum number of mice showing signal in a given area, namely, $n = 1$. The second level represented more than 50th percentile of mice with overlapping signal in a given area. Using the GNU Image Manipulation Program (GIMP), areas with fluorescent signal were delineated on templates taken from the Paxinos and Franklin mouse atlas. For the validation of AAV spread focused around ACA, we used the Paxinos and Franklin atlas to identify the boundaries of the ACA on any given slice, while the Allen Brain Atlas was used for our whole-brain rabies virus–based input mapping, which allowed us to define anterior-posterior spread better as it has a higher granularity of coronal slices.

Dendritic spine imaging and characterization

Images were acquired using an upright LSM780 Confocal microscope (Carl Zeiss). Following procedures previously described in (*5*), a nonbiased, whole-neuron approach was taken to characterize dendritic spines. Specifically, two neurons per animal were imaged on both the apical and basal dendrites. To qualify for spine analysis, whole neurons were selected that met the following requirements: (i) The neuron had to be filled and display spines at least up to 200 μm away from the soma on both apical and basal dendrites and (ii) display no overlapping of dendritic processes with other neuron processes. For the chemogenetic study, $mCherry^+$ and $mCherry^-$ neurons were defined as having >50% of soma pixels above 3 SD and below 2 SD of the mean image mCherry fluorescence intensity, respectively. Images were taken of sections from two basal dendrites and two apical dendrites from each neuron. Dendritic segments were imaged using a 100× lens (numerical aperture of 1.4; Carl Zeiss) and a zoom of 3.0. Images were taken with a resolution of 1024 × 300, pixel dwell time was 1.58 μm/s, and the line average was set to 8. Pixel size was 0.03 μm in the *x-y* plane and 0.01 μm in the *z* plane.

To assure consistency of imaging across difference confocal sessions, power was consistently set to 3.0%, and gain was adjusted within the range of 600 to 800 units to achieve consistent light intensity values within the same set of neurons. Images were deconvolved using a three-dimensional resolution enhancement with AutoDeblur software (Media Cybernetics) and then run through the dynamic range filter in Neuron Studio. For quantification, Neuron Studio was used to classify spines as thin, mushroom, or stubby on the basis of the head-to-neck ratio. Spines whose head-to-neck ratio was less than 1 were classified as thin spines, spines whose head-to-neck ratio was approximately 1 were classified as stubby spines, and spines whose head-to-neck ratio was greater than 1 were classified as mushroom spines. To accurately detect dendritic spines from background noise, puncta were only counted as spines if they moved into and out of the *z* plane with the dendritic branch. Spine density was calculated as the total spine count/dendritic length. All imaging and analysis were all performed by an author who remained agnostic to the group conditions until the analysis was completed.

Behavior: 5CSRTT

Behavior was conducted following procedures previously described in (*5*) using black plastic trapezoid Bussey-Saksida touch screen chambers [walls: 20 cm high by 18 cm wide (at screen-magazine) by 24 cm wide (at screen) by 6 cm wide (at magazine) (Lafayette Instrument)]. Stimuli were displayed on a touch-sensitive screen (30.7 cm, screen resolution of 600 × 800) divided into five response windows by a black plastic mask (4.0 × 4.0 cm, positioned centrally with windows spaced 1.0 cm apart and 1.5 cm above the floor) fitted in front of the touch screen. Schedules were designed, and data were collected and analyzed using ABET II Touch software (Lafayette Instrument). The inputs and outputs of the multiple chambers were controlled by WhiskerServer software (Lafayette Instrument). Before training on 5CSRTT, mice were initially trained to touch the screen. Mice were acclimated to the chambers for 3 days in 30-min sessions. During this habituation phase, the food magazine was illuminated, and diluted sweetened condensed milk (Eagle Brand) was dispensed every 40 s. Mice were then trained to touch the response windows. If the mouse touched the stimulus, then the milk reward was delivered in conjunction with a tone and magazine light. Touches to nonstimuli had no consequence. After reaching criterion on this phase (20 touches in 30 min for two consecutive days), mice moved onto 5CSRTT training phase. Mice were tested 5 days a week, 100 trials a day (or up to 30 min). Each trial began with the illumination of the magazine light. When the mouse made a nose poke in the food magazine, the stimulus was delivered after an intertrial interval (ITI) period of 5 s. If a mouse touched the screen during this ITI period, then the response was recorded as premature, and the mouse was punished with a 5-s time-out (house light on). After the time-out period, the magazine light illumination and house light switch off signaled onset of the next trial. After the ITI period, a stimulus appeared randomly in one of the five response windows for a set stimulus duration (this varied from 32 to 2 s). A limited-hold period followed by the stimulus duration was 5 s, during which the stimulus was absent but the mouse was still able to respond to the location. Responses during stimulus presence and limited-hold period could be recorded either as correct (touching the stimulus window) or incorrect (touching any other windows). A correct response was rewarded with a tone, as well as milk delivery, indicated by the illumination of the magazine light. A failure to respond to any window over the stimulus and limited-hold period was counted as an omission. Incorrect responses and omissions were punished with a 5-s time-out. In addition, animals could make perseverative responses that are screen touches after a correct or incorrect response. Animals started at stimulus duration of 32 s. With a goal to baseline mice at a stimulus duration of 2 s, the stimulus duration was sequentially reduced from 32, 16, 8, 4, to 2 s. Animals had to reach a criterion (<50 trials, <80% accuracy, and >20% omissions) over two consecutive days to pass from one stage to the next. After reaching baseline criterion with the 2-s stimulus duration (five consecutive days), mice were challenged with an increased attentional demand by reducing the stimulus duration to 2, 1.5, 1, and 0.8 s (reduced stimulus test). They then underwent 4 days of testing. Attention and response control were assessed by measuring the following performance: percent accuracy [100 × correct responses/(correct responses + incorrect responses)], percent omission [100 × omissions/(omissions + correct responses + incorrect responses)], percent premature response [100 × premature responses/(omissions + correct responses + incorrect responses)], percent perseverative response [100 × perseverative responses / (correct responses + incorrect responses)], latency to correct response, and latency to reward collection after correct choices.

Behavior: Progressive-ratio task

Following procedures previously described in (*5*), behavior was conducted after the completion of the 5CSRTT in touch screen chambers. In initial operant training, mice were trained to nose-touch the visual stimulus (white square, 100% luminance) at the center screen one time in each trial to receive a diluted sweetened condensed milk (Eagle Brand) reward as dispensed in the 5CSRTT. Touches to nonstimuli had no consequence. After reaching criterion of at least 30 completed trials in 30 min, mice moved onto fixed-ratio training. In fixed-ratio training, mice were trained to nose-touch the visual stimulus two, three, and then five times to get a reward. Mice were required to reach criterion for 1 day for fixed ratios of 2:1 and 3:1 and for 3 days for a fixed ratio of 5:1 before proceeding to progressive-ratio training and testing. Task parameters were identical for progressive-ratio training, except completion of each trial; the number of touches required to receive a reward was incremented on a linear +4 basis (i.e., 1, 5, 9, etc.). If no stimulus response or magazine entry in the presence of a delivered reward was detected for 5 min, then the session ended and the animal was removed from the chamber. Otherwise, the session ended after 30 min. Mice had to achieve a stabile "breakpoint" defined as the number of target location responses in the last successfully completed trial for 2 days before proceeding to progressive-ratio testing. In progressive-ratio testing, mice performed the progressive-ratio task using the same parameters as progressive-ratio training but were allowed 60 min to complete the session. Mice were baselined on Monday with progressive-ratio training to ensure consistent performance and tested for four consecutive days. Breakpoint across the 4 days was averaged to give each mouse on breakpoint score.

AAV vector construction

Lynx1 was amplified from a cDNA library derived from mouse cortex and subcloned into a pcDNA3.1(−) vector for an overexpression vector. For *Lynx1* KD vector, following procedures previously described in (*68*), we used short hairpin RNA (shRNA) vector with limited reported off-target effects, in which shRNA is

embedded into a larger endogenous microRNA loop that allows robust expression from RNA polymerase 2 promoters of an AAV vector to avoid the recently reported potential off-target effect by the use of acute short hairpin–based KD. Two oligonucleotides including shRNA sequence for *Lynx1* were subcloned into pcDNA6.2-GW/*EmGfp*-miR using BLOCK-iT Pol II miR RNAi Expression Vector Kit with EmGFP (Life Technologies). Subclonings were performed using an isothermal DNA assembly method (Gibson Assembly; New England Biolabs) and transformed into *Escherichia coli*. Colonies with correct insert were identified through DNA sequencing (Genewiz), cultured, and then isolated using the HiSpeed Midiprep Kit (QIAGEN). Expression was first examined by transfection of N2A cells in vitro to identify one of four sets of shRNAs for the robust *Lynx1* KD (CCTGTGAAGCAGTTGTCCATTGTGTCAGTCAGTGGCCAAAACACAATGGAGACA ACTGCTTCAC,TGCTGTGAAGCAGTTGTCTCCATTGTGTTTTGGCCACTGACTGACACAATGGACAACTGCTTCA; Life Technologies). To create the pAAV vector, an inverted bicistronic 2A sequence was inserted into pAAV-Ef1α-DIO-*eGfp*-WPRE-pA (Addgene no. 37084) upstream of *eGfp* by PCR linearization and overhang production on pAAV vector. The pcDNA3.1(−)-*Lynx1* vector was used as a template for the *Lynx1* insert, which was subsequently inserted into the pAAV-DIO-*eGfp*-2A vector as described above to create a pAAV-DIO-*eGfp-2A-Lynx1*-WPRE-pA vector (Lynx1 overexpression). pcDNA6.2-*mGfp*-miR-*Lynx1* vector was subcloned into pAAV-DIO-*eGfp-2A-Lypd6*-WPRE-pA vector to generate pAAV-DIO-*mGfp*-miR-*Lynx1* (*Lynx1* KD) vector. After sequence verification, a large culture and Maxiprep isolation produced a purified vector that was sent to the University of North Carolina viral core for viral packaging using an AAV8 serotype. To assay overexpression or KD of *Lynx1* through quantitative PCR (qPCR), RNA was isolated using the RNeasy Lipid Tissue Mini Kit (QIAGEN), and cDNA was produced. The cDNA was subjected to qPCR analysis using a TaqMan assay (Life Technologies) at the Icahn School of Medicine at Mount Sinai Quantitative PCR CORE facility to quantify *Lynx1* mRNA and β-*actin* mRNA.

Cannula infusions

Mice were trained on the 5CSRTT before guide cannula implantation surgeries. During surgery, burr holes targeting ACA on both hemispheres (A/P, +0.2 mm and M/L, ±0.2 mm relative to lambda) were made. Twenty-two–gauge guide cannulas (C313GS, Plastics One) were then implanted at the cortical surface and secured using Metabond (Parkell). Dummy cannula were placed into the guide cannula to prevent clogging. Nicotine hydrogen tartrate salt (Sigma-Aldrich, St. Louis, MO) was fully dissolved in physiological saline. Immediately before the 5CSRTT, 500 nl of nicotine solution (0.09 or 0.35 μg per side) or saline was infused bilaterally in ACA at a rate of 500 nl/min through a 28-gauge internal cannula (C313IS, Plastics One) that projected 0.7 mm below the dura. Following infusion, internal cannula was left in place for 1 min to allow for diffusion of drug from infusion site and reduce backflow.

Enrichment analyses

Transcriptomic data of adult *Lynx1* KO (>P60) and adult WT C57BL/6 (>P60) mice ($n = 3$, each group) primary visual cortex (V1) were downloaded (GSE89757), background-corrected, quantile-normalized, and $\log_2$-transformed with Limma, and then differential expression was calculated using RankProd. Differentially expressed genes at a false discovery rate of <0.25 were mapped to human using the Mouse Genome Informatics homology reference to yield a 332 genes *Lynx1* KO signature. GWAS and autism subtype gene sets were curated from the literature (table S2). The likelihood of genes shared between the *Lynx1* KO signature and a given GWAS/autism gene set was assessed by hypergeometric tests (HTSanalyzeR R package), using the intersection of all human orthologous genes expressed on the *Lynx1* KO microarray and all human genes (9656 genes) as a background. Enrichment analyses were conducted in R (version 3.2.2).

Statistical methods

Statistical analyses were performed using Prism 6.0 (GraphPad) and SAS v9.4 (SAS). The linear mixed models were used for experiments using patch-clamp recordings and dendritic spine analysis to evaluate the genotype or age differences that involved repeated measures within animals. Specifically, doubly repeated measure-mixed models with respect to neuron and dendrite were used for the dendritic spine models, which included main effects genotype (WT versus KO), age group (adult versus adolescent), spine type (thin, stubby, or mushroom), and the relevant two- and three-way interaction terms. Because the three-way interaction term was highly significant, stratified results by spine type were presented subsequently. For electrophysiological recordings, ranks were used instead of the actual data because of having excess close to zero values. Animals were treated as random effects. In all these models, the variances were allowed to be heterogeneous across different subgroups, as the descriptive data suggested. Degrees of freedom were adjusted on the basis of the Satterthwaite method. For 5SRTT behavior data, the animal specific accuracy rate and omission rate were first summarized for each of the four stimulus durations (2, 1.5, 1, and 0.8 s) and were analyzed using a linear mixed model using a two-way repeated measures analysis with stimulus duration (2, 1.5, 1, and 0.8 s) as within-subject factors, followed by Šídák's multiple comparisons test. In the analysis of other 5CSRTT data and progressive-ratio testing, an unpaired two-tailed *t* test was used. For input mapping and ratio comparisons, input numbers were first normalized to the number of starter cells within each animal before analyses. Input mapping analyses were completed by a two-way brain region by genotype models with repeated brain measures. Whenever *t* test was performed, unpaired two-tailed *t* test was used. All data are expressed as means ± SEM, and circles represent *n* values.

SUPPLEMENTARY MATERIALS

Supplementary material for this article is available at http://advances.sciencemag.org/cgi/content/full/7/10/eabe1527/DC1

View/request a protocol for this paper from *Bio-protocol*.

REFERENCES AND NOTES

1. T. Paus, M. Keshavan, J. N. Giedd, Why do many psychiatric disorders emerge during adolescence? *Nat. Rev. Neurosci.* **9**, 947–957 (2008).
2. F. S. Lee, H. Heimer, J. N. Giedd, E. S. Lein, N. Šestan, D. R. Weinberger, B. J. Casey, Mental health. Adolescent mental health—Opportunity and obligation. *Science* **346**, 547–549 (2014).
3. E. I. Knudsen, Fundamental components of attention. *Annu. Rev. Neurosci.* **30**, 57–78 (2007).
4. S. Zhang, M. Xu, T. Kamigaki, J. P. Hoang Do, W.-C. Chang, S. Jenvay, K. Miyamichi, L. Luo, Y. Dan, Long-range and local circuits for top-down modulation of visual cortex processing. *Science* **345**, 660–665 (2014).
5. E. M. Nabel, Y. Garkun, H. Koike, M. Sadahiro, A. Liang, K. J. Norman, G. Taccheri, M. P. Demars, S. Im, K. Caro, S. Lopez, J. Bateh, P. R. Hof, R. L. Clem, H. Morishita, Adolescent frontal top-down neurons receive heightened local drive to establish adult attentional behavior in mice. *Nat. Commun.* **11**, 3983 (2020).

6. J. Mollon, E. E. M. Knowles, S. R. Mathias, R. Gur, J. M. Peralta, D. J. Weiner, E. B. Robinson, R. E. Gur, J. Blangero, L. Almasy, D. C. Glahn, Genetic influence on cognitive development between childhood and adulthood. *Mol. Psychiatry* **26**, 656–665 (2021).
7. M. W. G. Dye, D. Bavelier, Differential development of visual attention skills in school-age children. *Vision Res.* **50**, 452–459 (2010).
8. K. Konrad, S. Neufang, C. M. Thiel, K. Specht, C. Hanisch, J. Fan, B. Herpertz-Dahlmann, G. R. Fink, Development of attentional networks: An fMRI study with children and adults. *Neuroimage* **28**, 429–439 (2005).
9. B. L. Keehn, E. Palmer, A. J. Lincoln, R.-A. Müller, Functional brain organization for visual search in ASD. *Austism Res.* **5**, 314–330 (2008).
10. A. Mazaheri, S. Coffey-Corina, G. R. Mangun, E. M. Bekker, A. S. Berry, B. A. Corbett, Functional disconnection of frontal cortex and visual cortex in attention-deficit/hyperactivity disorder. *Biol. Psychiatry* **67**, 617–623 (2010).
11. D. Hoops, C. Flores, Making dopamine connections in adolescence. *Trends Neurosci.* **40**, 709–719 (2017).
12. D. Suri, C. M. Teixeira, M. K. C. Cagliostro, D. Mahadevia, M. S. Ansorge, Monoamine-sensitive developmental periods impacting adult emotional and cognitive behaviors. *Neuropsychopharmacology* **40**, 88–112 (2015).
13. S. Zhang, M. Xu, W.-C. Chang, C. Ma, J. P. Hoang Do, D. Jeong, T. Lei, J. L. Fan, Y. Dan, Organization of long-range inputs and outputs of frontal cortex for top-down control. *Nat. Neurosci.* **19**, 1733–1742 (2016).
14. H. Morishita, J. M. Miwa, N. Heintz, T. K. Hensch, Lynx1, a cholinergic brake, limits plasticity in adult visual cortex. *Science* **330**, 1238–1240 (2010).
15. S. M. Kassam, P. M. Herman, N. M. Goodfellow, N. C. Alves, E. K. Lambe, Developmental excitation of corticothalamic neurons by nicotinic acetylcholine receptors. *J. Neurosci.* **28**, 8756–8764 (2008).
16. J. M. Miwa, T. R. Stevens, S. L. King, B. J. Caldarone, I. Ibanez-Tallon, C. Xiao, R. M. Fitzsimonds, C. Pavlides, H. A. Lester, M. R. Picciotto, N. Heintz, The prototoxin lynx1 acts on nicotinic acetylcholine receptors to balance neuronal activity and survival in vivo. *Neuron* **51**, 587–600 (2006).
17. N. Bukhari, P. N. Burman, A. Hussein, M. P. Demars, M. Sadahiro, D. M. Brady, S. E. Tsirka, S. J. Russo, H. Morishita, Unmasking proteolytic activity for adult visual cortex plasticity by the removal of Lynx1. *J. Neurosci.* **35**, 12693–12702 (2015).
18. M. Sajo, G. Ellis-Davies, H. Morishita, Lynx1 limits dendritic spine turnover in the adult visual cortex. *J. Neurosci.* **36**, 9472–9478 (2016).
19. T. Robbins, The 5-choice serial reaction time task: Behavioural pharmacology and functional neurochemistry. *Psychopharmacology* **163**, 362–380 (2002).
20. H. Koike, M. P. Demars, J. A. Short, E. M. Nabel, S. Akbarian, M. G. Baxter, H. Morishita, Chemogenetic inactivation of dorsal anterior cingulate cortex neurons disrupts attentional behavior in mouse. *Neuropsychopharmacology* **41**, 1014–1023 (2016).
21. M. G. White, M. Panicker, C. Mu, A. M. Carter, B. M. Roberts, P. A. Dharmasri, B. N. Mathur, Anterior cingulate cortex input to the claustrum is required for top-down action control. *Cell Rep.* **22**, 84–95 (2018).
22. J. D. Raybuck, T. J. Gould, The role of nicotinic acetylcholine receptors in the medial prefrontal cortex and hippocampus in trace fear conditioning. *Neurobiol. Learn. Mem.* **94**, 353–363 (2010).
23. M. R. Smith, P. Burman, M. Sadahiro, B. A. Kidd, J. T. Dudley, H. Morishita, Integrative analysis of disease signatures shows inflammation disrupts juvenile experience-dependent cortical plasticity. *eNeuro* **3**, ENEURO.0240-16.2016 (2016).
24. Schizophrenia Working Group of the Psychiatric Genomics Consortium, Biological insights from 108 schizophrenia-associated genetic loci. *Nature* **511**, 421–427 (2014).
25. N. R. Wray, S. Ripke, M. Mattheisen, M. Trzaskowski, E. M. Byrne, A. Abdellaoui, M. J. Adams, E. Agerbo, T. M. Air, T. M. F. Andlauer, S.-A. Bacanu, M. Bækvad-Hansen, A. F. T. Beekman, T. B. Bigdeli, E. B. Binder, D. R. H. Blackwood, J. Bryois, H. N. Buttenschøn, J. Bybjerg-Grauholm, N. Cai, E. Castelao, J. H. Christensen, T.-K. Clarke, J. I. R. Coleman, L. Colodro-Conde, B. Couvy-Duchesne, N. Craddock, G. E. Crawford, C. A. Crowley, H. S. Dashti, G. Davies, I. J. Deary, F. Degenhardt, E. M. Derks, N. Direk, C. V. Dolan, E. C. Dunn, T. C. Eley, N. Eriksson, V. Escott-Price, F. H. F. Kiadeh, H. K. Finucane, A. J. Forstner, J. Frank, H. A. Gaspar, M. Gill, P. Giusti-Rodríguez, F. S. Goes, S. D. Gordon, J. Grove, L. S. Hall, E. Hannon, C. S. Hansen, T. F. Hansen, S. Herms, I. B. Hickie, P. Hoffmann, G. Homuth, C. Horn, J.-J. Hottenga, D. M. Hougaard, M. Hu, C. L. Hyde, M. Ising, R. Jansen, F. Jin, E. Jorgenson, J. A. Knowles, I. S. Kohane, J. Kraft, W. W. Kretzschmar, J. Krogh, Z. Kutalik, J. M. Lane, Y. Li, Y. Li, P. A. Lind, X. Liu, L. Lu, D. J. MacIntyre, D. F. MacKinnon, R. M. Maier, W. Maier, J. Marchini, H. Mbarek, P. McGrath, P. McGuffin, S. E. Medland, D. Mehta, C. M. Middeldorp, E. Mihailov, Y. Milaneschi, L. Milani, J. Mill, F. M. Mondimore, G. W. Montgomery, S. Mostafavi, N. Mullins, M. Nauck, B. Ng, M. G. Nivard, D. R. Nyholt, P. F. O'Reilly, H. Oskarsson, M. J. Owen, J. N. Painter, C. B. Pedersen, M. G. Pedersen, R. E. Peterson, E. Pettersson, W. J. Peyrot, G. Pistis, D. Posthuma, S. M. Purcell, J. A. Quiroz, P. Qvist, J. P. Rice, B. P. Riley, M. Rivera, S. S. Mirza, R. Saxena, R. Schoevers, E. C. Schulte, L. Shen, J. Shi, S. I. Shyn, E. Sigurdsson, G. B. C. Sinnamon, J. H. Smit, D. J. Smith, H. Stefansson, S. Steinberg, C. A. Stockmeier, F. Streit, J. Strohmaier, K. E. Tansey, H. Teismann, A. Teumer, W. Thompson, P. A. Thomson, T. E. Thorgeirsson, C. Tian, M. Traylor, J. Treutlein, V. Trubetskoy, A. G. Uitterlinden, D. Umbricht, S. Van der Auwera, A. M. van Hemert, A. Viktorin, P. M. Visscher, Y. Wang, B. T. Webb, S. M. Weinsheimer, J. Wellmann, G. Willemsen, S. H. Witt, Y. Wu, H. S. Xi, J. Yang, F. Zhang; eQTLGen; 23andMe, V. Arolt, B. T. Baune, K. Berger, D. I. Boomsma, S. Cichon, U. Dannlowski, E. C. J. de Geus, J. R. De Paulo, E. Domenici, K. Domschke, T. Esko, H. J. Grabe, S. P. Hamilton, C. Hayward, A. C. Heath, D. A. Hinds, K. S. Kendler, S. Kloiber, G. Lewis, Q. S. Li, S. Lucae, P. F. A. Madden, P. K. Magnusson, N. G. Martin, A. M. McIntosh, A. Metspalu, O. Mors, P. B. Mortensen, B. Müller-Myhsok, M. Nordentoft, M. M. Nöthen, M. C. O'Donovan, S. A. Paciga, N. L. Pedersen, B. W. J. H. Penninx, R. H. Perlis, D. J. Porteous, J. B. Potash, M. Preisig, M. Rietschel, C. Schaefer, T. G. Schulze, J. W. Smoller, K. Stefansson, H. Tiemeier, R. Uher, H. Völzke, M. M. Weissman, T. Werge, A. R. Winslow, C. M. Lewis, D. F. Levinson, G. Breen, A. D. Børglum, P. F. Sullivan; Major Depressive Disorder Working Group of the Psychiatric Genomics Consortium, Genome-wide association analyses identify 44 risk variants and refine the genetic architecture of major depression. *Nat. Genet.* **50**, 668–681 (2018).
26. Autism Spectrum Disorders Working Group of The Psychiatric Genomics Consortium, Meta-analysis of GWAS of over 16,000 individuals with autism spectrum disorder highlights a novel locus at 10q24.32 and a significant overlap with schizophrenia. *Mol. Autism* **8**, 21 (2017).
27. E. Marouli, M. Graff, C. Medina-Gomez, K. S. Lo, A. R. Wood, T. R. Kjaer, R. S. Fine, Y. Lu, C. Schurmann, H. M. Highland, S. Rüeger, G. Thorleifsson, A. E. Justice, D. Lamparter, K. E. Stirrups, V. Turcot, K. L. Young, T. W. Winkler, T. Esko, T. Karaderi, A. E. Locke, N. G. D. Masca, M. C. Y. Ng, P. Mudgal, M. A. Rivas, S. Vedantam, A. Mahajan, X. Guo, G. Abecasis, K. K. Aben, L. S. Adair, D. S. Alam, E. Albrecht, K. H. Allin, M. Allison, P. Amouyel, E. V. Appel, D. Arveiler, F. W. Asselbergs, P. L. Auer, B. Balkau, B. Banas, L. E. Bang, M. Benn, S. Bergmann, L. F. Bielak, M. Blüher, H. Boeing, E. Boerwinkle, C. A. Böger, L. L. Bonnycastle, J. Bork-Jensen, M. L. Bots, E. P. Bottinger, D. W. Bowden, I. Brandslund, G. Breen, M. H. Brilliant, L. Broer, A. A. Burt, A. S. Butterworth, D. J. Carey, M. J. Caulfield, J. C. Chambers, D. I. Chasman, Y.-D. I. Chen, R. Chowdhury, C. Christensen, A. Y. Chu, M. Cocca, F. S. Collins, J. P. Cook, J. Corley, J. C. Galbany, A. J. Cox, G. Cuellar-Partida, J. Danesh, G. Davies, P. I. W. de Bakker, G. J. de Borst, S. de Denus, M. C. H. de Groot, R. de Mutsert, I. J. Deary, G. Dedoussis, E. W. Demerath, A. I. den Hollander, J. G. Dennis, E. D. Angelantonio, F. Drenos, M. Du, A. M. Dunning, D. F. Easton, T. Ebeling, T. L. Edwards, P. T. Ellinor, P. Elliott, E. Evangelou, A.-E. Farmaki, J. D. Faul, M. F. Feitosa, S. Feng, E. Ferrannini, M. M. Ferrario, J. Ferrieres, J. C. Florez, I. Ford, M. Fornage, P. W. Franks, R. Frikke-Schmidt, T. E. Galesloot, W. Gan, I. Gandin, P. Gasparini, V. Giedraitis, A. Giri, G. Girotto, S. D. Gordon, P. Gordon-Larsen, M. Gorski, N. Grarup, M. L. Grove, V. Gudnason, S. Gustafsson, T. Hansen, K. M. Harris, T. B. Harris, A. T. Hattersley, C. Hayward, L. He, I. M. Heid, K. Heikkilä, Ø. Helgeland, J. Hernesniemi, A. W. Hewitt, L. J. Hocking, M. Hollensted, O. L. Holmen, G. K. Hovingh, J. M. M. Howson, C. B. Hoyng, P. L. Huang, K. Hveem, M. A. Ikram, E. Ingelsson, A. U. Jackson, J.-H. Jansson, G. P. Jarvik, G. B. Jensen, M. A. Jhun, Y. Jia, X. Jiang, S. Johansson, M. E. Jørgensen, T. Jørgensen, P. Jousilahti, J. W. Jukema, B. Kahali, R. S. Kahn, M. Kähönen, P. R. Kamstrup, S. Kanoni, J. Kaprio, M. Karaleftheri, S. L. R. Kardia, F. Karpe, F. Kee, R. Keeman, L. A. Kiemeney, H. Kitajima, K. B. Kluivers, T. Kocher, P. Komulainen, J. Kontto, J. S. Kooner, C. Kooperberg, P. Kovacs, J. Kriebel, H. Kuivaniemi, S. Küry, J. Kuusisto, M. L. Bianca, M. Laakso, T. A. Lakka, E. M. Lange, L. A. Lange, C. D. Langefeld, C. Langenberg, E. B. Larson, I.-T. Lee, T. Lehtimäki, C. E. Lewis, H. Li, J. Li, R. Li-Gao, H. Lin, L.-A. Lin, X. Lin, L. Lind, J. Lindström, A. Linneberg, Y. Liu, Y. Liu, A. Lophatananon, J. Luan, S. A. Lubitz, L.-P. Lyytikäinen, D. A. Mackey, P. A. F. Madden, A. K. Manning, S. Männistö, G. Marenne, J. Marten, N. G. Martin, A. L. Mazul, K. Meidtner, A. Metspalu, P. Mitchell, K. L. Mohlke, D. O. Mook-Kanamori, A. Morgan, A. D. Morris, A. P. Morris, M. Müller-Nurasyid, P. B. Munroe, M. A. Nalls, M. Nauck, C. P. Nelson, M. Neville, S. F. Nielsen, K. Nikus, P. R. Njølstad, B. G. Nordestgaard, I. Ntalla, J. R. O'Connel, H. Oksa, L. M. Olde Loohuis, R. A. Ophoff, K. R. Owen, C. J. Packard, S. Padmanabhan, C. N. A. Palmer, G. Pasterkamp, A. P. Patel, A. Pattie, O. Pedersen, P. L. Peissig, G. M. Peloso, C. E. Pennell, M. Perola, J. A. Perry, J. R. B. Perry, T. N. Person, A. Pirie, O. Polasek, D. Posthuma, O. T. Raitakari, A. Rasheed, R. Rauramaa, D. F. Reilly, A. P. Reiner, F. Renström, P. M. Ridker, J. D. Rioux, N. Robertson, A. Robino, O. Rolandsson, I. Rudan, K. S. Ruth, D. Saleheen, V. Salomaa, N. J. Samani, K. Sandow, Y. Sapkota, N. Sattar, M. K. Schmidt, P. J. Schreiner, M. B. Schulze, R. A. Scott, M. P. Segura-Lepe, S. Shah, X. Sim, S. Sivapalaratnam, K. S. Small, A. V. Smith, J. A. Smith, L. Southam, T. D. Spector, E. K. Speliotes, J. M. Starr, V. Steinthorsdottir, H. M. Stringham, M. Stumvoll, P. Surendran, L. M. 't Hart, K. E. Tansey, J.-C. Tardif, K. D. Taylor, A. Teumer, D. J. Thompson, U. Thorsteinsdottir, B. H. Thuesen, A. Tönjes, G. Tromp, S. Trompet, E. Tsafantakis, J. Tuomilehto, A. Tybjaerg-Hansen, J. P. Tyrer, R. Uher, A. G. Uitterlinden, S. Ulivi, S. W. van der Laan, A. R. Van Der Leij, C. M. van Duijn, N. M. van Schoor, J. van Setten, A. Varbo, T. V. Varga, R. Varma, D. R. Velez Edwards, S. H. Vermeulen, H. Vestergaard, V. Vitart, T. F. Vogt, D. Vozzi, M. Walker, F. Wang, C. A. Wang, S. Wang, Y. Wang, N. J. Wareham, H. R. Warren, J. Wessel, S. M. Willems, J. G. Wilson, D. R. Witte, M. O. Woods, Y. Wu, H. Yaghootkar, J. Yao, P. Yao,

L. M. Yerges-Armstrong, R. Young, E. Zeggini, X. Zhan, W. Zhang, J. H. Zhao, W. Zhao, W. Zhao, H. Zheng, W. Zhou; EPIC-InterAct Consortium; CHD Exome+ Consortium; ExomeBP Consortium; T2D-Genes Consortium; GoT2D Genes Consortium; Global Lipids Genetics Consortium; ReproGen Consortium; MAGIC Investigators, J. I. Rotter, M. Boehnke, S. Kathiresan, M. I. McCarthy, C. J. Willer, K. Stefansson, I. B. Borecki, D. J. Liu, K. E. North, N. L. Heard-Costa, T. H. Pers, C. M. Lindgren, C. Oxvig, Z. Kutalik, F. Rivadeneira, R. J. F. Loos, T. M. Frayling, J. N. Hirschhorn, P. Deloukas, G. Lettre, Rare and low-frequency coding variants alter human adult height. *Nature* **542**, 186–190 (2017).

28. J. C. Darnell, S. J. Van Driesche, C. Zhang, K. Y. S. Hung, A. Mele, C. E. Fraser, E. F. Stone, C. Chen, J. J. Fak, S. W. Chi, D. D. Licatalosi, J. D. Richter, R. B. Darnell, FMRP stalls ribosomal translocation on mRNAs linked to synaptic function and autism. *Cell* **146**, 247–261 (2011).
29. S. W. Kong, M. Sahin, C. D. Collins, M. H. Wertz, M. G. Campbell, J. D. Leech, D. Krueger, M. F. Bear, L. M. Kunkel, I. S. Kohane, Divergent dysregulation of gene expression in murine models of fragile X syndrome and tuberous sclerosis. *Mol. Autism* **5**, 1–11 (2014).
30. S. Ben-Shachar, M. Chahrour, C. Thaller, C. A. Shaw, H. Y. Zoghbi, Mouse models of MeCP2 disorders share gene expression changes in the cerebellum and hypothalamus. *Hum. Mol. Genet.* **18**, 2431–2442 (2009).
31. N. J. M. van Beveren, L. C. Krab, S. Swagemakers, G. Buitendijk, E. Boot, P. van der Spek, Y. Elgersma, T. A. M. J. van Amelsvoort, Functional gene-expression analysis shows involvement of schizophrenia-relevant pathways in patients with 22q11 deletion syndrome. *PLOS ONE* **7**, e33473 (2012).
32. T. A. Lanz, E. Guilmette, M. M. Gosink, J. E. Fischer, L. W. Fitzgerald, D. T. Stephenson, M. T. Pletcher, Transcriptomic analysis of genetically defined autism candidate genes reveals common mechanisms of action. *Mol. Autism* **4**, 45 (2013).
33. T. M. Kazdoba, P. T. Leach, J. L. Silverman, J. N. Crawley, Modeling fragile X syndrome in the Fmr1 knockout mouse. *Intractable Rare Dis. Res.* **3**, 118–133 (2014).
34. C. E. M. Golden, M. S. Breen, L. Koro, S. Sonar, K. Niblo, A. Browne, N. Burlant, D. Di Marino, S. De Rubeis, M. G. Baxter, J. D. Buxbaum, H. Harony-Nicolas, Deletion of the KH1 domain of Fmr1 leads to transcriptional alterations and attentional deficits in rats. *Cereb. Cortex* **29**, 2228–2244 (2019).
35. D. D. Krueger, E. K. Osterweil, S. P. Chen, L. D. Tye, M. F. Bear, Cognitive dysfunction and prefrontal synaptic abnormalities in a mouse model of fragile X syndrome. *Proc. Natl. Acad. Sci. U.S.A.* **108**, 2587–2592 (2011).
36. J. Moon, A. E. Beaudin, S. Verosky, L. L. Driscoll, M. Weiskopf, D. A. Levitsky, L. S. Crnic, B. J. Strupp, Attentional dysfunction, impulsivity, and resistance to change in a mouse model of fragile X syndrome. *Behav. Neurosci.* **120**, 1367–1379 (2006).
37. D. B. Bailey Jr., M. Raspa, M. Olmsted, D. B. Holiday, Co-occurring conditions associated with FMR1 gene variations: Findings from a national parent survey. *Am. J. Med. Genet. A* **146A**, 2060–2069 (2008).
38. K. M. Cornish, F. Munir, G. Cross, Differential impact of the FMR-1 full mutation on memory and attention functioning: A neuropsychological perspective. *J. Cogn. Neurosci.* **13**, 144–150 (2001).
39. B. Xu, Y. Zhang, S. Zhan, X. Wang, H. Zhang, X. Meng, W. Ge, Proteomic profiling of brain and testis reveals the diverse changes in ribosomal proteins in fmr1 knockout mice. *Neuroscience* **371**, 469–483 (2018).
40. S. Das Sharma, J. B. Metz, H. Li, B. D. Hobson, N. Hornstein, D. Sulzer, G. Tang, P. A. Sims, Widespread alterations in translation elongation in the brain of juvenile Fmr1 knockout mice. *Cell Rep.* **26**, 3313–3322.e5 (2019).
41. R. G. Ross, S. K. Hunter, L. McCarthy, J. Beuler, A. K. Hutchison, B. D. Wagner, S. Leonard, K. E. Stevens, R. Freedman, Perinatal choline effects on neonatal pathophysiology related to later schizophrenia risk. *Am. J. Psychiatry* **170**, 290–298 (2013).
42. E. Gould, N. J. Woolf, L. L. Butcher, Postnatal development of cholinergic neurons in the rat: I. Forebrain. *Brain Res. Bull.* **27**, 767–789 (1991).
43. X. Zhang, C. Liu, H. Miao, Z.-h. Gong, A. Nordberg, Postnatal changes of nicotinic acetylcholine receptor α2, α3, α4, α7 and β2 subunits genes expression in rat brain. *Int. J. Dev. Neurosci.* **16**, 507–518 (1998).
44. E. Proulx, M. Piva, M. K. Tian, C. D. C. Bailey, E. K. Lambe, Nicotinic acetylcholine receptors in attention circuitry: The role of layer VI neurons of prefrontal cortex. *Cell. Mol. Life Sci.* **71**, 1225–1244 (2014).
45. C. J. Heath, M. R. Picciotto, Nicotine-induced plasticity during development: Modulation of the cholinergic system and long-term consequences for circuits involved in attention and sensory processing. *Neuropharmacology* **56** (suppl. 1), 254–262 (2009).
46. A. E. Takesian, L. J. Bogart, J. W. Lichtman, T. K. Hensch, Inhibitory circuit gating of auditory critical-period plasticity. *Nat. Neurosci.* **21**, 218–227 (2018).
47. K. Guillem, B. Bloem, R. B. Poorthuis, M. Loos, A. B. Smit, U. Maskos, S. Spijker, H. D. Mansvelder, Nicotinic acetylcholine receptor β2 subunits in the medial prefrontal cortex control attention. *Science* **333**, 888–891 (2011).
48. P. Artoni, A. Piffer, V. Vinci, J. LeBlanc, C. A. Nelson, T. K. Hensch, M. Fagiolini, Deep learning of spontaneous arousal fluctuations detects early cholinergic defects across neurodevelopmental mouse models and patients. *Proc. Natl. Acad. Sci. U.S.A.* **117**, 23298–23303 (2020).
49. L. Petreanu, T. Mao, S. M. Sternson, K. Svoboda, The subcellular organization of neocortical excitatory connections. *Nature* **457**, 1142–1145 (2009).
50. A. Cruz-Martin, M. Crespo, C. Portera-Cailliau, Delayed stabilization of dendritic spines in fragile X mice. *J. Neurosci.* **30**, 7793–7803 (2010).
51. A. B. Patel, K. W. Loerwald, K. M. Huber, J. R. Gibson, Postsynaptic FMRP promotes the pruning of cell-to-cell connections among pyramidal neurons in the L5A neocortical network. *J. Neurosci.* **34**, 3413–3418 (2014).
52. A. Asiminas, A. D. Jackson, S. R. Louros, S. M. Till, T. Spano, O. Dando, M. F. Bear, S. Chattarji, G. E. Hardingham, E. K. Osterweil, D. J. A. Wyllie, E. R. Wood, P. C. Kind, Sustained correction of associative learning deficits after brief, early treatment in a rat model of fragile X syndrome. *Sci. Transl. Med.* **11**, eaao0498 (2019).
53. W. S. Sossin, "Fragile" equilibrium between translation and transcription. *Proc. Natl. Acad. Sci. U.S.A.* **115**, 12086–12088 (2018).
54. C. Bagni, R. S. Zukin, A synaptic perspective of fragile X syndrome and autism spectrum disorders. *Neuron* **101**, 1070–1088 (2019).
55. J. B. Dictenberg, S. A. Swanger, L. N. Antar, R. H. Singer, G. J. Bassell, A direct role for FMRP in activity-dependent dendritic mRNA transport links filopodial-spine morphogenesis to fragile X syndrome. *Dev. Cell* **14**, 926–939 (2008).
56. P.-Y. Deng, Z. Rotman, J. A. Blundon, Y. Cho, J. Cui, V. Cavalli, S. S. Zakharenko, V. A. Klyachko, FMRP regulates neurotransmitter release and synaptic information transmission by modulating action potential duration via BK channels. *Neuron* **77**, 696–711 (2013).
57. M. R. Brown, J. Kronengold, V. R. Gazula, Y. Chen, J. G. Strumbos, F. J. Sigworth, D. Navaratnam, L. K. Kaczmarek, Fragile X mental retardation protein controls gating of the sodium-activated potassium channel Slack. *Nat. Neurosci.* **13**, 819–821 (2010).
58. M. D'Antuono, D. Merlo, M. Avoli, Involvement of cholinergic and gabaergic systems in the fragile X knockout mice. *Neuroscience* **119**, 9–13 (2003).
59. S. Chang, S. M. Bray, Z. Li, D. C. Zarnescu, C. He, P. Jin, S. T. Warren, Identification of small molecules rescuing fragile X syndrome phenotypes in Drosophila. *Nat. Chem. Biol.* **4**, 256–263 (2008).
60. S. R. Thomson, S. S. Seo, S. A. Barnes, S. R. Louros, M. Muscas, O. Dando, C. Kirby, D. J. A. Wyllie, G. E. Hardingham, P. C. Kind, E. K. Osterweil, Cell-type-specific translation profiling reveals a novel strategy for treating fragile X syndrome. *Neuron* **95**, 550–563.e5 (2017).
61. S. R. Kesler, A. A. Lightbody, A. L. Reiss, Cholinergic dysfunction in fragile X syndrome and potential intervention: A preliminary 1H MRS study. *Am. J. Med. Genet. A* **149A**, 403–407 (2009).
62. J. L. Bruno, S. H. Hosseini, A. A. Lightbody, M. K. Manchanda, A. L. Reiss, Brain circuitry, behavior, and cognition: A randomized placebo-controlled trial of donepezil in fragile X syndrome. *J. Psychopharmacol.* **33**, 975–985 (2019).
63. J. K. Sahu, S. Gulati, S. Sapra, R. Arya, S. Chauhan, M. R. Chowdhury, N. Gupta, M. Kabra, Y. K. Gupta, S. N. Dwivedi, V. Kalra, Effectiveness and safety of donepezil in boys with fragile x syndrome: A double-blind, randomized, controlled pilot study. *J. Child Neurol.* **28**, 570–575 (2013).
64. P. Barttfeld, B. Wicker, S. Cukier, S. Navarta, S. Lew, M. Sigman, A big-world network in ASD: Dynamical connectivity analysis reflects a deficit in long-range connections and an excess of short-range connections. *Neuropsychologia* **49**, 254–263 (2011).
65. D. R. Dajani, L. Q. Uddin, Local brain connectivity across development in autism spectrum disorder: A cross-sectional investigation. *Autism Res.* **9**, 43–54 (2016).
66. L. K. Bicks, K. Yamamuro, M. E. Flanigan, J. M. Kim, D. Kato, E. K. Lucas, H. Koike, M. S. Peng, D. M. Brady, S. Chandrasekaran, K. J. Norman, M. R. Smith, R. L. Clem, S. J. Russo, S. Akbarian, H. Morishita, Prefrontal parvalbumin interneurons require juvenile social experience to establish adult social behavior. *Nat. Commun.* **11**, 1003 (2020).
67. M. P. Demars, H. Morishita, Cortical parvalbumin and somatostatin GABA neurons express distinct endogenous modulators of nicotinic acetylcholine receptors. *Mol. Brain* **7**, 75 (2014).
68. M. Sadahiro, M. P. Demars, P. Burman, P. Yevoo, A. Zimmer, H. Morishita, Activation of somatostatin interneurons by nicotinic modulator Lypd6 enhances plasticity and functional recovery in the adult mouse visual cortex. *J. Neurosci.* **40**, 5214–5227 (2020).

Acknowledgments: We thank N. Heintz (Rockefeller University) for providing *Lynx1* KO mice, as well as D. Kiraly, M. Baxter, S. Espeso-Gil, S. Akbarian, and members of the Morishita laboratory for helpful feedback. **Funding:** This work was funded by NIH F30MH111143, Seaver Foundation to E.N.F., NIH F31MH121010 to K.J.N., and NIH R21NS105119, R21MH106919, R01EY024918, and R01MH119523 to H.M. **Author contributions:** E.N.F. and H.M. designed experiments. E.N.F. and H.M. wrote the manuscript with contributions from all coauthors. Y.G. performed slice electrophysiology. E.N.F. and G.T. performed spine analysis. E.N.F., K.J.N., Y.G., and S.I. performed rabies virus input mapping. S.I., J.S., M.P.D.,

and E.N.F. performed in situ hybridization. M.P.D. made and validated virus vectors. E.N.F., K.J.N., M.P.D., and Y.G. conducted viral injections. E.N.F., K.J.N., M.P.D., J.S., K.C., S.E.M., C.C., H.K., and P.M. performed behavioral experiments. M.R.S. and E.N.F. conducted informatics analysis. E.N.F., S.I., J.B., L.W., and M.J. performed viral and cannula placement validation. E.N.F., K.J.N., Y.G., H.-M.L., and H.M. performed statistical analysis. H.M. supervised the research. **Competing interests:** The authors declare that they have no competing interests. **Data and materials availability:** All data needed to evaluate the conclusions in the paper are present in the paper and/or the Supplementary Materials. All other data and analysis are available from the corresponding author upon reasonable request.

Submitted 12 August 2020
Accepted 21 January 2021
Published 5 March 2021
10.1126/sciadv.abe1527

Citation: E. N. Falk, K. J. Norman, Y. Garkun, M. P. Demars, S. Im, G. Taccheri, J. Short, K. Caro, S. E. McCraney, C. Cho, M. R. Smith, H.-M. Lin, H. Koike, J. Bateh, P. Maccario, L. Waltrip, M. Janis, H. Morishita, Nicotinic regulation of local and long-range input balance drives top-down attentional circuit maturation. *Sci. Adv.* **7**, eabe1527 (2021).